Shear-driven formation of olivine veins by dehydration of ductile serpentinite: a numerical study with implications for transient weakening

Stefan M. Schmalholz[1], Evangelos Moulas[2], Ludovic Räss[3,4] and Othmar Müntener[1]

[1]Institute of Earth Sciences, University of Lausanne, 1015 Lausanne, Switzerland

[2]Institut of Geosciences and Mainz Institute of Multiscale Modeling (M^3ODEL), Johannes Gutenberg University of Mainz, Germany

[3] Laboratory of Hydraulics, Hydrology and Glaciology (VAW), ETH Zurich, Zurich, Switzerland

[4]Swiss Federal Institute for Forest, Snow and Landscape Research (WSL), Birmensdorf, Switzerland

Email, corresponding author: Stefan Schmalholz (`stefan.schmalholz@unil.ch`)

Evangelos Moulas: `evmoulas@uni-mainz.de`; Ludovic Räss: `luraess@ethz.ch`;

Othmar Müntener: Othmar.Muntener@unil.ch

Key points:

- During viscous simple-shearing of serpentinite, en-échelon olivine veins form by dehydration and grow in direction parallel to compression
- Vein formation is a self-limiting process and kinetic reaction rate must be faster than fluid-pressure diffusion rate to form olivine
- Porosity evolution is controlled by three mechanisms: volume change, temporal solid density variation and reactive mass transfer

Abstract

Serpentinite subduction and the associated formation of dehydration veins is important for subduction zone dynamics and water cycling. Field observations suggest that en-échelon olivine veins in serpentinite mylonites formed by dehydration during simultaneous shearing of ductile serpentinite. Here, we test a hypothesis of shear-driven formation of dehydration veins with a two-dimensional hydro-mechanical-chemical numerical model. We consider the reaction antigorite + brucite = forsterite + water. Shearing is viscous and the shear viscosity decreases exponentially with porosity. The total and fluid pressures are initially homogeneous and in the antigorite stability field. Initial perturbations in porosity, and hence viscosity, cause fluid pressure perturbations. Dehydration nucleates where the fluid pressure decreases locally below the thermodynamic pressure defining the reaction boundary. Dehydration veins grow during progressive simple-shearing in a direction parallel to the maximum principal stress, without involving fracturing. The porosity evolution associated with dehydration reactions is controlled to approximately equal parts by three mechanisms:

volumetric deformation, solid density variation and reactive mass transfer. The temporal evolution of dehydration veins is controlled by three characteristic time scales for shearing, mineral-reaction kinetics and fluid-pressure diffusion. The modelled vein formation is self-limiting and slows down due to fluid flow decreasing fluid pressure gradients. Mineral-reaction kinetics must be significantly faster than fluid-pressure diffusion to generate forsterite during vein formation. The self-limiting feature can explain the natural observation of many, small olivine veins and the absence of few, large veins. We further discuss implications for transient weakening during metamorphism and episodic tremor and slow-slip in subduction zones.

Plain language summary

Serpentinite is a rock that contains water which is bound within the crystal lattice. When serpentinite is plunging together with tectonic plates into the Earth mantle, the changing pressure and temperature conditions cause chemical reactions which releases the water bound in the crystal lattice; a process called dehydration. A typical mineral that forms by dehydration is olivine. Dehydration is important for the global water cycle, since much water is transferred with tectonic plates into the mantle and is migrating back to the Earth surface after dehydration. However, many aspects of the water cycle remain still unclear, since dehydration during plunging of tectonic plates involves the incompletely understood interaction of three fundamental mechanical and chemical processes: mechanical deformation of the rock, porous flow of released fluid and chemical reactions involving changes in rock density. Here, we present a new mathematical model to investigate the coupled processes of rock deformation, fluid flow and dehydration reactions. We present computer simulations which can explain why the dehydration occurs in narrow and elongated regions which are termed veins. We propose that our simulations could explain the observation of many small olivine veins in strongly sheared serpentinite.

1. Introduction

The dehydration of serpentinite at subduction zones is an important process for the global water cycle (e.g., Peacock, 1990; Pettke and Bretscher, 2022; Ulmer and Trommsdorff, 1995; Rupke et al., 2004), for the dynamics and seismicity at subduction zones (e.g., Bloch et al., 2018; Hacker et al., 2003) or for arc magmatism due to hydration of the mantle wedge (e.g., Hebert et al., 2009; John et al., 2012). More generally, the interaction of mineral reactions, fluid flow and rock deformation is important for a variety of geodynamic processes, such as chemical and volatile cycling (e.g., Bebout, 2014) or reaction-induced weakening of faults and shear zones (e.g., Labrousse et al., 2010; Sulem and Famin, 2009), as well as for practical applications such as natural carbon storage (e.g., Matter and Kelemen, 2009) or geothermal energy exploitation (e.g., Pandey et al., 2018). However, many aspects of the coupling of mineral reactions, fluid flow and rock deformation are still unclear.

Indirect observations that have been attributed to serpentinite dehydration at

subduction zones are aseismic episodic tremor and slow-slip (ETS) phenomena (e.g., Burlini et al., 2009; Tarling et al. 2019). These phenomena are commonly thought to result from episodic fault slip, likely facilitated or promoted by pulses of fluid release associated with fluid pressure variations (e.g., Audet et al., 2009; Connolly, 1997; Frank et al., 2015; Gomberg et al., 2010; Shelly et al., 2006; Taetz et al., 2018). For example, such slow-slip occurs on the plate interface in Cascadia at 30 to 40 km depth (e.g., Gomberg et al., 2010) and for temperatures probably between 400 and 500 °C (e.g., Tarling et al., 2019 and references therein). However, how the dehydration reaction, the associated fluid release and the volumetric and shear deformation of the involved rocks are coupled and actually cause the episodic slow-slip phenomena remains elusive.

Direct observation of the dehydration of serpentinite at subduction zones is not possible in nature. However, field observations in areas with abundant exposed serpentinites at variable pressure and temperature may provide insight into incipient dehydration stages. In the European Alps, exposed serpentinites, which experienced variable peak pressures and temperatures, are abundant in many regions. Examples are the serpentinites of Saas Zermatt (Western Alps) or of the Erro-Tobbio unit (Voltri massif, Ligurian Alps, Italy; e.g., Hermann et al., 2000; Peters et al., 2020; Plümper et al., 2017; Scambelluri et al. 1991, Scambelluri et al., 1995; Kempf et al., 2020). These serpentinite bearing regions are key areas that preserve ductile and brittle structures that are related to fluid release. The serpentinites of the Erro-Tobbio unit exhibit olivine-bearing veins and the metamorphic olivine most likely results from the breakdown of antigorite and brucite (Fig. 1; e.g., Hermann et al., 2000; Plümper et al., 2017; Scambelluri et al., 2004). The olivine veins occur in two settings: as minimally deformed veins within little deformed, variably serpentinized peridotite and as deformed veins within strongly deformed antigorite serpentinite, described as a serpentinite mylonite (Fig. 1; e.g., Hermann et al., 2000; Plümper et al., 2017). These serpentinite mylonites are cut by en-échelon olivine veins, which in turn are dissected by multiple sets of olivine-bearing shear bands (Hermann et al., 2000). Plümper et al. (2017) suggest that the association of undeformed and sheared veins attests that dehydration-induced vein formation was synchronous with ductile deformation in the enclosing serpentinite mylonites. Furthermore, Hermann et al. (2000) hypothesize that (i) multiple sets of olivine shear bands provide evidence for continuous deformation, (ii) sheared olivine-rich veins are probably very weak due to continuous solution and precipitation in the presence of a fluid phase, (iii) fluid produced by the dehydration reaction was (partially) trapped in the serpentinite mylonite and (iv) serpentinite mylonites are not only zones with highly localized deformation but also zones of focused fluid flow. However, these coupled physical-chemical hypotheses for olivine vein formation have not been tested with theoretical models based on the concepts of continuum mechanics and thermodynamics. Recently, Huber et al. (2022) presented a hydro-chemical (HC) model to study the formation of olivine veins in dehydrating serpentinite. However, they do not consider any solid-mechanical aspects of olivine vein formation and do, hence, not consider volumetric or shear defor-

mation of the serpentinite and associated fluid pressure changes. Therefore, we cannot apply their model to test the coupled physical-chemical hypothesis of shear-driven olivine vein formation.

Here, we test the hydrological, mechanical and chemical feasibility of a hypothesis for the formation of observed olivine veins in serpentinite mylonites with a new two-dimensional (2D) hydro-mechanical-chemical (HMC) model. The hypothesis is (Fig. 2): During viscous shearing of serpentinite, the magnitudes of ambient pressure and temperature were close to the magnitudes required for triggering the dehydration reaction from serpentinite to olivine (Fig. 3A). The effective viscosity of serpentinite was spatially variable, for example due to variable porosity or heterogeneities in mineralogy (Fig. 2A). Weak domains, with lower viscosity, cause pressure variations in the sheared serpentinite so that the dehydration reactions are triggered in domains with locally decreased pressure. The dehydration forms olivine and increases the porosity locally, which in turn increases the size of weak domains, consisting of an olivine-fluid mixture. The dehydration region forms vein-like structures that grow in a direction parallel to the maximal compressive stress without any fracturing (Fig. 2A and B). After fluid has escaped the olivine-rich region, the olivine-rich veins, observable in the field, have formed (Fig. 2C). We test this hypothesis with a 2D HMC model because such models are suitable to theoretically study the coupling between chemical reactions, fluid flow and deformation (e.g., Kolditz et al., 2015; Poulet et al., 2012). Such coupled models have been applied to study a variety of geodynamic processes, for example, reaction-driven cracking during serpentinization (e.g., Evans et al., 2020), porosity evolution and clogging during serpentinization (e.g. Malvoisin et al., 2021), the impact of dehydration on earthquake nucleation (e.g., Brantut et al., 2011), the impact of shear heating and associated chemical rock decomposition on thrusting (e.g., Poulet et al., 2014) or reactive melt migration (e.g., Aharonov et al., 1997; Baltzell et al., 2015; Bessat et al., 2022; Schiemenz et al., 2011). We apply here an extension of a HMC model that was previously used to model the dehydration reaction: brucite = periclase + water (Schmalholz et al., 2020). Here, we elaborate this HMC model and consider a simple MgO-SiO_2-H_2O (MSH) system for the reaction: antigorite + brucite = forsterite + water (Fig. 3). For simplicity, we consider an isothermal system and a fixed chemical composition so that the reaction antigorite + brucite = forsterite + water is balanced everywhere in the model domain.

The main aim of our study is to better understand the fundamental coupling of dehydration reactions, fluid flow and rock deformation, for which a simplified model is useful. Particular aims of our study are (1) to test the hypothesis for the shear-driven formation of olivine veins, (2) to quantify the mechanisms that control the porosity evolution and fluid pressure during dehydration of rocks and (3) to quantify the impact of shearing rate and kinetic reaction rate on the growth of dehydration veins.

2. Mathematical model

2.1. Porous medium densities

We consider a simple MSH system and the reaction antigorite ($Mg_{48}Si_{34}O_{85}(OH)_{62}$) + 20 brucite ($Mg(OH)_2$) = 34 forsterite ($Mg_2SiO_4$) + 51 water ($H_2O$). We assume that antigorite and brucite together represent one solid rock phase with a homogeneous solid density, (in kg/m^3), and homogeneous material properties. All model parameters and variables are presented in Table 1. The total density of the porous rock, either consisting of antigorite + brucite or forsterite + water, is

with porosity (volume ratio) and pore-fluid density . For simplicity, we assume that the solid phase consists of two components, (1) the non-volatile components, MgO and SiO_2, that remain always in the solid and (2) the volatile component, H_2O, that is liberated during dehydration. We quantify the amount of the non-volatile component as a function of MgO inside the solid with its solid mass (in kg) fraction, , which is (68 times the molar mass of MgO / (68 times the molar mass of MgO + 51 times the molar mass of H_2O)) for the solid made of antigorite + brucite in a molar ratio of 1/20. Equivalently, for forsterite. We neglect the SiO_2 in the calculations, because the SiO_2 for the considered reaction cannot vary independently from MgO. The relative density of the solid MgO component in the solid phase is

2.2. Hydro-chemical model

The conservation of mass (per unit volume) of the solid and the fluid is given by respectively (e.g., McKenzie, 1984)

where is time, is the divergence operator, and are vectors of the fluid and solid barycentric velocities, respectively, and is a dehydration rate that quantifies the rate at which mass is transferred from the solid to the fluid phase. Concerning the symbols for vector and tensor quantities, we use indices and as superscripts, because vector and tensor components will have additional subscripts indicating the spatial direction, and scalar quantities can be easier distinguished from vector and tensor quantities. Here, we do not use two separate mass conservation equations for solid and fluid, but use the conservation equation of total mass which results from the sum of equations and (e.g., Fowler, 1985; Beinlich et al., 2020; Malvoisin et al., 2021; Plümper et al., 2016; Schmalholz et al., 2020):

The relative velocity of the fluid to the solid, , in equation is expressed by Darcy's law in the absence of gravity

where is the permeability coefficient in a Kozeny–Carman-type permeability expression, is the fluid viscosity and is the fluid pressure. We need two mass conservation equations because we consider two phases, solid and fluid. In addition to the conservation of total mass, we use the conservation of the total non-volatile component (MgO) which is described by

.

There is no fluid velocity in this conservation equation because we assume that the dissolution of MgO in the fluid is negligible.

We consider a constant temperature and a closed system with constant system composition for the whole model domain, however, H_2O can migrate within our model domain. It has been experimentally demonstrated that dehydration reactions are controlled by fluid pressure (e.g., Llana-Fúnez et al., 2012) and, therefore, we approximate , and as a function of , which is expressed as (Schmalholz et al., 2020):

,

whereby the values of , and for a range of values of are calculated by equilibrium Gibbs free-energy minimization (e.g., Connolly, 2005, 2009; Fig. 3), using the thermodynamic dataset of Holland and Powell (1998). We assume that always corresponds to , as a result of its equation of state (Fig. 3C). Due to the sharp, step-like variation of and with varying across the dehydration reaction (Fig. 3C and D) we assume that the reaction is controlled by a kinetic reaction timescale, so that values of do not change instantaneously if crosses the value of the reaction pressure at 12.65 kbar (Fig. 3). The kinetic reaction timescales relevant to thermodynamic equilibrium are (e.g., Omlin et al., 2017)

where t_{kin} is the characteristic kinetic timescale. Employing an effective kinetic timescale for the considered reaction allows us to quantify the impact of reaction kinetics on the model results. Furthermore, the simulations are numerically more stable because the kinetic formulation resolves better the temporal transition of the reaction and prohibits potentially strong density oscillations for numerical grid points where values of are very close to the reaction pressure.

2.3. Mechanical model

The solid part of the 2D porous medium is behaving in a visco-plastic manner under shear deformation. We assume that the shear viscosity is an exponential function of the porosity (e.g., Schmeling et al., 2012). There are other possible porosity-viscosity relations, but for simplicity we apply here only one of these relations. The relations between the deviatoric stress tensor components, (where are the components of the total stress tensor, is total pressure and is the Kronecker delta) and solid velocity gradients, or deviatoric strain rate tensor components , are then

where subscripts and are either 1 (representing the horizontal x-direction) or 2 (representing the vertical y-direction), is the reference solid shear viscosity for the initial porosity, , and . The represents the effective, porosity-dependent shear viscosity of the porous rock. The factor 30 was determined by experiments with olivine-melt mixtures (e.g., Schmeling et al., 2012). We further apply for one simulation a von Mises yield stress, , to limit the maximal value of the deviatoric stresses. The square root of the second invariant of the deviatoric stress tensor, controls a plastic multiplier, . If , then deviatoric stresses are modified using

.

This von Mises plasticity prohibits that stresses locally increase to unrealistically

high values. Furthermore, we consider a poro-visco-elastic volumetric deformation for which the divergence of the solid velocity field is a function of total pressure, , and fluid pressure, (e.g., Yarushina and Podladchikov, 2015):

where is the bulk viscosity, is the drained bulk modulus, and with being the solid bulk modulus. The applied equations for conservation of total linear momentum (or force balance equations) without inertial forces and gravity are

2.4. Governing system of equations

The above equations represent a system of 11 equations for 11 unknowns, which are , , , , , , , , , and , assuming that the deviatoric stress tensor is symmetric, . The deviatoric stress tensor components, , and , are calculated using equations . The solid and fluid densities and the mass fraction are calculated from the fluid pressure using equation (see also equation below and Fig. 3C and D). Equation is used to determine the fluid pressure, , equation to determine total pressure, , equation to determine the porosity, , and the two force balance equations to determine the two solid velocities, and . To determine , , , and we employ the iterative pseudo-transient (PT) finite difference method described in detail in Schmalholz et al. (2020). The PT equations are

.

When the discrete PT time derivatives of the left-hand sides of the equations converge towards zero during iterations, then the corresponding steady-state equations on the right-hand sides are solved. The closed system of governing equations is given by equations , , and .

2.5. Model configuration

We assume that and are initially identical. The porosity is 2%, except in an elliptical region in the model center where the porosity exhibits a Gaussian distribution with a maximal value of 16% (Fig. 4). The initial Gaussian distribution of the porosity is: . The distance controls the width, or variance, of the porosity distribution which has an elliptical form with an axis ratio of 2 and with the long axis parallel to the vertical y-direction (Fig. 4). The origin of the coordinate system is at the center of the elliptical region with positive coordinates indicating towards the right side and upwards (Fig. 4). The shear and bulk viscosities are smaller in the central region due to the higher porosity. We assume a constant temperature of 500 °C for which the thermodynamic reaction pressure in our model is at 12.65 kbar (Fig. 3). The exact temperature value is not essential for our isothermal study, because the variation of the solid and fluid densities with varying fluid pressure is similar for temperatures between 450 and 550 °C (Fig. 3A and B). The initial values of and are everywhere equal to 12.75 kbar, which is a pressure value slightly above the thermodynamic reaction pressure (Fig. 3A and B). We apply far-field simple shear for the boundary velocities (Fig. 4) so that the divergence, or volume change, of the entire model domain is zero. Shearing is parallel to the horizontal x-direction and, hence, orthogonal to the long axis of the elliptical region with elevated porosity (Fig.

4). Boundary conditions for and are of Dirichlet type, with boundary values fixed to the initial ambient values.

2.6. Numerical algorithm and dimensionless parameters

All partial derivatives are approximated with discrete difference ratios following the standard procedure of staggered finite difference (FD) methods (e.g., Gerya, 2019). The numerical algorithm consists of an outer time loop containing an internal PT iteration loop (Schmalholz et al., 2020). The PT iteration procedure aims at minimizing the PT time derivatives, i.e. the left-hand sides in the discretized equations . The iteration procedure is stopped when the PT time derivatives reach a predefined tolerance, here 10^{-8}. The iterative implicit PT solution of the discretised system of equations requires the definition of four numerical pseudo time steps, , namely, , , , and to solve for , , , and and , respectively. The physical time step, , controls the evolution of the system in physical time for which we implicitly solve. The applied numerical time steps are specified in appendix A1.

There are many possibilities to scale and non-dimensionalize the model parameters inside the numerical algorithm. We programmed the numerical algorithm in such a way that the specific magnitudes of individual parameters, such as shear viscosity, are not significant and that the characteristic physical behaviour of the system is controlled by dimensionless parameters. This scaling provided also the most stable convergence during the PT iterations. The applied dimensionless parameters and numerical examples applied in the simulations are:

where is the model width and is the applied far-field simple shear rate (Fig. 4). The values of the applied parameters are discussed in section 4.

For reasons of numerical efficiency, we approximate the thermodynamic relations of the densities and mass fractions with the fluid pressure, obtained with Gibbs free-energy minimization, with analytical functions (Fig. 3C and D):

where is the reaction pressure, here 12.65 kbar. We use the functions above in the numerical algorithm to calculate densities and mass fraction from the current fluid pressure.

3. Results

3.1. Scaling and presentation of results

We present most quantities in dimensionless form to emphasize their general validity. For example, all distances are made dimensionsless by dividing them by and all times are made dimensionless by dividing them with the characteristic time . Consequently, all velocities are made dimensionless by dividing them by the characteristic velocity . In contrast, since we consider a particular metamorphic reaction, we display the densities and pressures in dimensional units.

3.2. Dehydration vein formation under simple shear

For the first simulation presented here, we use the dimensionless parameters and specific parameter values given in equation . The numerical resolution is 900×900 grid points in the x- and y-direction, respectively. A numerical resolution test is given in appendix A2. The coupling of the dehydration reaction, fluid flow and solid deformation is controlled by four characteristic time scales: a time scale related to fluid pressure diffusion, , a time scale related to the applied far-field deformation, , a time scale related to the mineral-reaction kinetics, (equation), and a time scale related to viscoelastic stress relaxation, . We assume here = 10^{11} Pa which, for the parameter values in equation , yields ~ 10^{-3} and indicates that the deformation is effectively viscous since is significantly shorter than . The ratio is commonly referred to as Deborah number (e.g. Reiner, 1964; Moulas et al., 2019). For the first simulation, = 0.071 and = 0.0025 so that both the characteristic times for shearing and reaction kinetics are shorter than the characteristic time of diffusive fluid flow. The ratio is similar to a Damköhler number since it relates the characteristic time of mineral reactions to the characteristic time of transport by diffusive fluid flow. The central region with initially higher porosity (Fig. 5E) represents a mechanically weak inclusion because the shear and bulk viscosity decrease with increasing porosity. The applied far-field simple shear causes variations in around the weak region and the numerical results for the first time step show two regions in which is smaller than the reaction pressure of 12.65 kbar (black contours in Fig. 5A). Therefore, dehydration is triggered in these two regions of decreased . The dehydration causes the release of water, consequently an increase in porosity and, hence, a decrease of viscosity. With progressive simple shearing these dehydrating regions grow in the direction parallel to the maximal principal stress, , which is oriented 45 degrees with respect to the shearing direction (Fig. 5E). The maximal and minimal, , principal stresses have been calculated using the algorithm of Spitz et al. (2020), which was originally developed to calculate principal strain directions. During progressive shearing, two dehydrating regions evolve and form vein-like regions with increased values of and (Fig. 5). The total solid velocity field (grey arrows in Fig. 5A to D) indicates the applied far-field simple shear and local deviations from the horizontal shear direction. For the specific parameters given in equation the maximal shear stresses are ca. 125 MPa. We also calculate the distance between the highest (in vertical y-direction) and the lowest point on the contours for = 12.65 kbar (red straight lines in Fig 5A to D). We will use this distance as a proxy for the change in length of the dehydrating region representing the length of the dehydration vein. During progressive shearing, the value of in the dehydration region increases from initially ca. 2550 kg m^{-3} to ca. 3100 kg m^{-3} which represents the transformation from antigorite + brucite to forsterite (Figs. 3C and 5A to D). In the region of the two forsterite veins, the associated values of increase from initially 2% to ca. 60% (Fig. 5E to H). Two representative contours of , for 5 and 15%, highlight two features of the evolution of : the growth of high-porosity dehydration veins and the clock-wise rotation of the initial porosity field due to the applied simple shear (Fig. 5E to H).

3.3. Dehydration vein formation for faster deformation rate and plastic yield stress

We perform a second simulation with the same parameters as the first simulation, except that we apply now a different value of which provides = 0.038 (Fig. 6A to D) generating a faster shearing since the characteristic time of deformation is shorter. The main difference to the simulation with = 0.071 (Fig. 5) is that the two dehydration regions connect during progressive shearing to form a single dehydration vein (Fig. 6D). For the specific parameters given in equation the maximal shear stresses are ca. 220 MPa. We perform a third simulation with the same parameters as in the second simulation and apply a von Mises yield stress of 150 MPa (Fig. 6E to H). With such yield stress, a single dehydration vein also forms but the vein is shorter and thicker for the same simulated times (Fig. 6). The performed three simulations result in a similar development of dehydration veins with forsterite, but show that different deformation rates and the application of a yield stress impact the geometry and length of the veins.

3.4. Coupling of dehydration reaction, fluid flow and solid deformation

To better understand and visualize the coupling between the dehydration reaction, fluid flow and solid deformation we show the distribution and evolution of various quantities on a single figure (Fig. 7). We use the results of the first simulation (Fig. 5) and we focus on one dehydration region in the area to the top-left of the model center (Fig. 7). The divergence of the solid velocity, , indicates a volumetric change associated with dehydration vein formation (Fig. 7). A positive value of indicates volume increase, or dilation (blue colors in Fig. 7). Overall, the solid velocities indicate the applied far-field simple shear deformation (blue arrows in Fig. 7), with some deviations around the dehydrating region. The fluid velocities (red arrows in Fig. 7) are completely different compared to the solid velocities. For the first time step, fluid flow only occurs in the central region where the porosity, and hence permeability, is high (Fig. 7A). During dehydration vein formation, fluid flow mainly occurs in the region of the veins where significant dilation takes places (Fig. 7B to D). The fluid velocities indicate fluid flow from the boundary of the dehydrating region towards the centre of the vein (Fig. 7C). In other words, fluid is released during dehydration from the surrounding serpentinite and the released fluid flows into the vein. For the first time step, the porosity distribution indicates the initial, Gaussian-type, porosity distribution (blue contours in Fig. 7). With progressive deformation and vein formation, the high-porosity region grows in the direction of the dehydration vein, indicated by significant dilation and fluid flow. At the beginning of shearing, a larger region with fluid pressure (red contours in Fig. 7) <12.65 kbar corresponds more or less to the region of significant dilation (Fig. 7A). The solid densities (dashed grey contours in Fig. 7) increase during the progressive dehydration reaction and the transformation from antigorite + brucite to forsterite (Fig. 7B to D). The values of solid density increase with time due to the applied mineral-reaction kinetics which avoids that the density changes instantaneously once the fluid pressure decreases locally below 12.65

kbar. With progressive vein formation, fluid pressures below 12.65 kbar only exist in the region of significant dilation, fluid flow and increased values of solid density (Fig. 7).

3.5. Mechanisms controlling porosity variation and fluid pressure

In our coupled HMC model, the temporal variation of porosity is controlled by several mechanisms, such as volumetric deformation of the solid or mass transfer due to the dehydration reaction. To quantify the relative contribution of the mechanisms controlling the temporal variation of porosity, we post-process our numerical results (i.e. calculate values from saved numerical results). We quantify the mass transfer rate, , associated with the dehydration reaction, which can be expressed by (using equation):

.

Note that in equation the material time derivative (, including the advection term,) is used and, hence, the divergence term is different compared to equation . Therefore, equation represents an approximation of since the advective term is not taken into account, here for simplicity of the post-processing. Equation can be rearranged to provide an expression for the temporal variation of the porosity:

Equation shows that the temporal variation of the porosity is controlled by three mechanisms: (1) volumetric deformation of the solid (i.e. divergence of velocity field; first term on right-hand side of equation), (2) temporal variation of solid density (second term) and (3) mass transfer of H_2O from the solid to the fluid phase associated with the dehydration reaction (third term). We display the spatial distribution of the four terms in equation for the first simulation at a dimensionless time of 0.7 (Fig. 8). The temporal variation of porosity, quantified by the term on the left-hand side of equation , is positive and largest in the region of increased porosity, indicating an increase in porosity with time (Fig. 8A). Each of the three terms on the right-hand side of equation can be calculated from the saved numerical results (Fig. 8C to E) and their sum (Fig. 8B) provides essentially the same result as the term on the left-hand side of equation (Fig. 8A). The results show that the magnitudes of the relative contributions of volume change (Fig. 8C), solid density variation (Fig. 8D) and mass transfer (Fig. 8E) to the temporal variation of porosity are similar. Therefore, volume change, solid density variation and mass transfer equally contribute to the porosity variation and, hence, for the evolution of the dehydration veins.

We also investigate the porosity variation for a simulation which has the same value of = 0.071 as the first simulation, but with a slower kinetic-reaction rate (or longer reaction time) of = 0.022 for a dimensionless time of 1.0 (Fig. 9). The magnitude of the temporal porosity variation is now slower (compare Fig. 8A and 9A) but the relative contribution of volume change, solid density variation and mass transfer to the porosity variation is again similar. Therefore, different kinetic reaction rates change the magnitude of the temporal porosity variation,

but do not change the relative importance of volume change, density variation and mass transfer controlling the porosity evolution.

Similar to the temporal variation of , the distribution of is also controlled by several mechanisms and variables. To quantify the mechanisms controlling , we post-process again our numerical results. Substituting equation , which defines , into equation and solving for yields

.

Equation shows that is controlled by five mechanisms and quantities: (1) the magnitude of (first term on the right-hand side of equation), (2) elastic deformation involving the temporal variation of and (second term), (3) temporal variations in porosity (third term), (4) temporal variations of solid density (fourth term) and (5) mass transfer by dehydration (fifth term). We display the spatial distribution of all terms in equation for the first simulation at a dimensionless time of 0.7 (Fig. 10). The distribution of is mainly controlled by the distribution of (Fig. 10A and C). The distribution of can be accurately post-processed by summing up the five terms on the right-hand side of equation (Fig. 10B). The mass transfer (Fig. 10E), the porosity variation (Fig. 10F) and the solid density variation (Fig. 10G) have an approximately equal impact on the distribution of , but their contributions are significantly smaller compared to the contribution of . The contribution of elastic volumetric deformation (Fig. 10H) is essentially negligible, since it is three orders of magnitude smaller than the magnitude of . For the presented simulation, the maximal value of the deviatoric stress invariant, (equation), in the model domain is ca. 140 MPa (Fig. 10D).

3.6. Impact of kinetic reaction rate and shearing rate on vein evolution

We performed in total ten simulations to investigate the impact of the far-field shearing rate and of the kinetic reaction rate on the evolution of dehydration veins and forsterite generation (Fig. 11). Six simulations had the same value of $= 0.0025$ but different values of (legend in Fig. 11A). The increase in length of the red line shown in figure 5A to D is used as a proxy for the temporal evolution of the vein length (Fig. 5A). The initial value of vein length is determined by the initial distribution of (Fig. 5A). In regions with $<$12.65 kbar the dehydration reaction is triggered, which causes a local increase of H_2O and an increase of (Fig. 11B). For the six simulations, this initial increase of generated values of $>$12.65 kbar everywhere in the model domain, so that the vein length is zero (Fig. 11A and B). With progressive deformation, values of decrease again below 12.65 kbar initiating the growth of a dehydration vein. The time until values of decrease below 12.65 kbar is longest for the simulation with the slowest far-field deformation rate (Fig. 11A). Consequently, the increase of starts latest for the simulation with slowest far-field deformation rate (Fig. 11C). However, during significant increase of the rate of increase (indicated by the slope of the density versus time lines) of is similar for all simulations, because they considered the same mineral-kinetic rate ($= 0.0025$). The simulation with the

fastest deformation rate (Fig. 6A to D; blue line in Fig. 11A to C) was run a second time, but then with a von Mises yield stress (Fig. 6E to F; dashed blue line in Fig. 11A to C). The application of the yield stress slows down the vein growth, but has no significant impact on the evolution of (Fig. 11C). The temporal evolution of the vein length shows that the veins grow fast at the onset of vein formation and then vein growth slows down progressively (Fig. 11A) because the minimum values of in the model increase progressively (Fig. 11B) due to ongoing fluid flow which reduces gradients of .

We performed four simulations for the same value of = 0.071 but for four different values of (legend in Fig. 11D). The vein growth is similar for the four simulations (Fig. 11D), however, the increase of is significantly different due to the different mineral-reaction rates (Fig. 11F). The values of increase fastest for the fastest reaction rate (Fig. 11F), but values of vary less during deformation for faster reaction rates (Fig. 11E). For slow reaction kinetics, = 0.022 (Fig. 11F), maximal values of did not reach 2800 kg m^{-3} hindering the complete formation of forsterite when the vein growth has essentially stopped (corresponding blue line in Fig. 11D). The results for different kinetic rates suggest that the kinetic reaction rate must be significantly faster than the pressure diffusion rate to allow the complete transformation from antigorite + brucite to forsterite during dehydration and vein growth, while fluid pressures are in the forsterite stability field.

4. Discussion

The performed simulations show that it is hydrologically, mechanically and chemically feasible to form olivine veins by dehydration reactions during ductile shearing of serpentinite. In the scenario studied here, dehydration is shear-driven and triggered by fluid pressure perturbations caused by heterogeneities in porosity-dependent effective viscosity. The resulting veins grow in a direction parallel to the maximal principal stress and no fracturing is required for vein formation and growth. The simulations show that the two dimensionless ratios and control the temporal evolution of the dehydration vein length, the fluid pressure and the solid density (Fig. 11). In our simulations both the values of and need to be significantly shorter than (Fig. 11). To test the applicability of our simulations to sheared serpentinite at subduction zones, we estimate the value of using the parameter values specified in equation and the initial porosity of 2%. The least constrained parameter in is likely the effective permeability, , which in our simulations would be = . Experimental studies suggest that serpentinite permeability decreases exponentially with depth and is in the order of 10^{-23} and 10^{-21} m^2 at a depth of 7 km below seafloor (e.g. Hatakeyama et al., 2017). Using the extrapolation of Hatakeyama et al. (2017) (their equation 1) for their sepertinite termed Sengen-03 provides a permeability of 10^{-30} m^2 for a confining pressure of 9 kbar and 10^{-35} m^2 for a confining pressure of 12.75 kbar, as applied here. Therefore, an effective permeability in the order of 10^{-27} m^2, as used here, seems not unrealistic for serpentinite under a confining pressure of 12.75 kbar and the assumed temperature of 500 °C. For simplicity, we

assume here an isotropic permeability, but in natural serpentinite the permeability might be anisotropic. For the considered parameter values we obtain = 4 kyr. A representative value of in our simulations is (Fig. 11A). The inverse of corresponds to the applied far-field shearing rate, , which is then . A shear strain rate in the order of is feasible for serpentinite shearing at a subduction plate interface (e.g. Chernak and Hirth, 2010). A representative value of in our simulations forming forsterite is (Fig. 11D) which corresponds to 4 years. Here, we assume a viscosity of serpentinite of 10^{18} Pas. Despite the importance of serpentinite, its rheology at lithospheric-scale pressure and temperature conditions remains not well constrained (David et al., 2018; Hirauchi et al., 2020, and references therein). However, for the ambient pressure and temperature conditions considered here, viscosities of serpentinite between 10^{17} and 10^{18} Pas seem feasible based on experimental studies (e.g., Chernak and Hirth, 2010; Hilairet et al., 2007). For the applied parameter values, the characteristic time, , is ca. 12 days. The dimensionless simulation times for the ten simulations are between 600 and 1500 (Fig. 11) which then corresponds to a real time between approximately 20 and 50 years, respectively.

We consider here, for simplicity, a fixed chemical composition for which forsterite + water results from dehydration of antigorite + brucite + a negligible amount of free water. We consider this negligle amount of free water simply to be able to calculate thermodynamically the fluid density in the stability field of antigorite + brucite (Fig. 3C). Natural chemical compositions, in for example the Erro-Tobbio unit, are more complex and feature a higher chemical variability as considered in our model. However, the main aim of our study is to investigate the fundamental coupling between dehydration reactions, fluid flow and rock deformation, justifying the use of a simplified MSH system. Our model suggests that natural areas of serpentinite dehydration, consisting of olivine and water, are mechanically weak due to their high, up to 60%, porosity and water content. After the formation of the dehydration veins, the water eventually escapes the dehydration region, so that finally only olivine is left in the veins.

Field data show that in the Erro Tobbio region the olivine in the veins is metamorphic olivine which resulted from the dehydration of serpentinite. A dehydration origin of the olivine is supported by geochemical studies (e.g., Kempf et al., 2020; Peters et al., 2020). Furthermore, the particular en-échelon orientation of the olivine veins suggest that the vein orientation is controlled by the stress field associated with the serpentinite shearing (Hermann et al. 2000). Therefore, based on published geochemical studies and structural observations we propose that the formation of observed olivine veins was the result of a coupled deformation-reaction process that accelerated the mineral dehydration along particular orientations, controlled by the local stress field in the sheared serpentinite. Similar veins made of metamorphic olivine have been described from subducted serpentinite, such as in the Zermatt-Saas unit in the Central Alps (e.g., Kempf et al., 2020).

The initial distribution of porosity in the presented simulations is simple and

defined by a Gaussian distribution. Such a simple initial porosity distribution is again useful to study the fundamental coupling of dehydration reactions and rock deformation. More realistic would likely be an initial random distribution of porosity. To test whether the studied formation of dehydration veins also occurs for a more realistic initial porosity distribution, we performed one simulation with an initial random porosity distribution. The initial values of porosity vary randomly between 2 and 16% in the model domain. We generated the initial porosity distribution with the random field generator presented in Räss et al. (2019). For this simulation, we applied = 0.012 and = 8.2×10^{-4}. Furthermore, the initial values for and are 12.73 kbar. All other parameters are identical to the values of the first simulation (Fig. 5). The simulation shows that during shearing many dehydration veins with increasing solid density and porosity are formed, similar to the simulations with an initial Gaussian porosity distribution (Fig. 12). Particularly, despite the variability in shape of the dehydrating regions, the longest axis of the dehydrating regions always grows in the direction of the maximum principal stress. Hence, the results with an initial random porosity distribution suggest that the investigated simulations with an initial Gaussian porosity distribution capture the first-order mechanisms of shear-driven dehydration vein formation for more complex and natural model configurations. Furthermore, the simulation shows the formation of many veins with similar length which is similar to observations from natural olivine veins (Fig. 1A to C). The generation of many similar veins results from the self-limiting nature of vein growth (Fig. 11A and D) which prohibits the generation of few large veins.

The presented model could potentially be applied to investigate fluid-related processes causing episodic tremor and slow-slip events (ETS; e.g., Peng & Gomberg 2010). Despite the lack of consensus on the inter-relationships between mineral dehydration, fluid flow, critical stress and ETS, the coincidence of the location of low-frequency earthquakes to regions with high Vp/Vs ratios requires the consideration of fluid flow and mineral dehydration in these settings (e.g., Burlini et al. 2009; Kato et al. 2010; Shelly et al. 2006; Van Avendonk et al., 2010). For example, Van Avendonk et al. (2010) infer a zone of very high Vp/Vs ratio of 6 at the top of the subducting Cocos slab between 35 and 55 km depth, lying downdip of the seismogenic zone. They propose that these high Vp/Vs ratios are due to several-meter thick shear zones under high pore pressure and that the hydrous pore fluids were generated by prograde dehydration reactions. The 35 to 55 km depth range with inferred high Vp/Vs ratios corresponds to the depth range and ambient pressure considered in our model. In addition, the correlation of rapid-tremor migration to pore-pressure waves suggests that this coincidence can be explained by the coupled processes of dehydration, fault weakening and tremor migration (Cruz-Atienz et al. 2018). Thus, the formation of fluid-filled veins, as modelled here, can be correlated to the transient weakening that is inferred in regions of mineral dehydration. Furthermore, the dehydration reaction, generating olivine-fluid bearing veins, and the subsequent fluid escape, leaving behind olivine-only veins, will cause a viscosity inversion:

when significant fluid is present in the olivine bearing veins, then the effective viscosity of the olivine-fluid veins is smaller than the viscosity of the serpentinite; but once the fluid has escaped the veins the effective viscosity of the olivine-only veins is larger than the viscosity of the serpentinte. We expect that, under the presence of a general anisotropic stress field, the vein formation will lead to an increase of the anisotropic effective viscosity of the subducted mantle rocks as a result of the different effective viscosities of serpentinite and olivine + fluid assemblages. When the fluid is completely drained from these veins, the viscosity contrast between olivine and serpentinite is such that the associated anisotropy will be permanent.

5. Conclusions

We present a hydro-mechanical-chemical model to investigate the reaction antigorite + brucite = forsterite + water. The model can explain shear-driven formation of dehydration veins in ductile serpentinite and, hence, supports the hypothesis of shear-driven formation of metamorphic olivine veins in the serpentinites of the Erro Tobbio unit (Fig. 1). Vein formation is triggered by fluid pressure perturbations caused by local perturbations of a porosity-dependent effective viscosity. The veins consist of a weak forsterite-water mixture and grow in a direction parallel to the maximal principal stress which is controlled by the applied far-field simple shearing. The modelled growth of the dehydration veins is not a stable or runaway process but a self-limiting process because the fluid pressure perturbations that drive the vein growth decrease during progressive shearing due to fluid flow.

In our model, three characteristic time scales control the formation of dehydration veins: (1) The time scale of fluid pressure diffusion, t_{dif}, which controls porous fluid flow via Darcy's law, (2) the time scale of the far-field shearing, t_{def}, which is the inverse of the far-field shearing rate and (3) the time scale of the mineral-reaction kinetics, t_{kin}, which controls the time to achieve thermodynamic equilibrium. To form an olivine (here forsterite) vein, the kinetic reaction rate for the transformation from serpentinite to olivine must be fast enough so that olivine can form during vein growth, while significant fluid pressure perturbations exist. The numerical simulations suggest that the kinetic reaction rate should be at least two orders of magnitude faster than the characteristic rate of fluid pressure diffusion.

In our models, the temporal evolution of porosity during dehydration is controlled by three mechanisms: solid volume change, solid density variation and reactive mass transfer. All three mechanisms have a similar impact on the porosity evolution. Hence, our model shows that deformation of the solid rock should be considered when quantifying dehydration vein formation. The fluid pressure distribution is mainly controlled by the total pressure distribution. Mass transfer, porosity variation and solid density variation impact the fluid pressure distribution to a minor extend and only in the dehydrating region.

The presented model can help to understand the formation of olivine veins in

serpentinite mylonites in subduction zones. Such veins are observed in several high pressure serpentinites in the Western Alps and Liguria. The modelled veins have a similar orientation as natural en-échelon olivine veins in serpentinite mylonite. The self-limiting feature of the modelled vein growth might also explain the natural observation of many smaller olivine veins and the absence of few large olivine veins. Furthermore, the presented model can explain transient weakening during dehydration in deforming rock which may be an important process during episodic tremor and slow-slip observed in subduction zones.

Acknowledgements

S.M.S. is grateful for theoretical advices from Y. Podladchikov and for practical programming help of T. Duretz. This work was supported by the University of Lausanne. E.M. acknowledges the Johannes Gutenberg University of Mainz for financial support. L.R. acknowledges financial support from the Swiss University Conference and the Swiss Council of Federal Institutes of Technology through the Platform for Advanced Scientific Computing (PASC) program, obtained via the PASC project GPU4GEO. There is no conflict of interest.

Availability Statement

The software developed and used in the scope of this study is licensed under MIT License. The latest versions of the code is available for download from GitHub at: https://github.com/PTsolvers/PseudoTransientHMC.jl (last access: 18 May 2022). Past and future versions of the software are available from a permanent DOI repository (Zenodo) at: https://doi.org/10.5281/zenodo.6559431 (Schmalholz and Räss, 2022). The codes are written using the Julia programming language and execute on graphical processing units (GPUs). Refer to the repository's README for additional information.

Appendix

A1. Pseudo-transient time steps

To solve the system of equations iteratively, we apply the following physical, , pseudo-transient (PT), , time steps:

(A1)

where and are horizontal and vertical numerical grid spacing, respectively. More information concerning the choice of such PT time steps can be found in Wang et al. (2022).

A2. Numerical resolution test

We present here the results of a numerical resolution test. Such test is essential to determine whether the evolution of the dehydrating region is independent of the employed numerical resolution. We performed the first simulation (Fig. 5) with the following different numerical resolutions: 150×150, 300×300, 500×500, 700×700 and 900×900 grid points (Fig. A1). For a dimensionless model time of 950, the ratio of the mean porosity in the model domain divided by the mean

porosity for a simulation with 900 × 900 grid points is plotted versus the corresponding resolution for simulations with different resolution (Fig. A1A). Similar ratios are plotted for the minimum fluid pressure in the model domain and the vein length. The higher the resolution, the less the three ratios vary, indicating the convergence of the numerical results upon increasing numerical resolution. The evolution of the minimum fluid pressure in the model domain with time is shown for different numerical resolutions (Fig. A1B). With larger numerical resolution, the temporal evolution of the minimum fluid pressure varies less, indicating again the convergence of the numerical results for increasing numerical resolution. Finally, the spatial distribution of at a dimensionless time of 785 is displayed for three different resolutions (Fig. A1C to E). For a resolution of 150×150 the contours of are jagged, confirming an insufficient numerical resolution (Fig. A1C). For numerical resolutions of 500×500 and 900×900 the contours of are smooth and the colormaps of cannot be distinguished by eye (Fig. A1D and E).The numerical resolution test shows that the applied numerical model provides results which converge for increasing numerical resolution and are, hence, not dependent on the numerical resolution.

References

Aharonov, E., M. Spiegelman, and P. Kelemen (1997), Three-dimensional flow and reaction in porous media: Implications for the Earth's mantle and sedimentary basins, Journal of Geophysical Research-Solid Earth, 102(B7), 14821-14833, doi:10.1029/97jb00996.

Aharonov, E., J. A. Whitehead, P. B. Kelemen, and M. Spiegelman (1995), Channeling instability of upwelling melt in the mantle, Journal of Geophysical Research-Solid Earth, 100(B10), 20433-20450, doi:10.1029/95jb01307.

Audet, P., M. G. Bostock, N. I. Christensen, and S. M. Peacock (2009), Seismic evidence for overpressured subducted oceanic crust and megathrust fault sealing, Nature, 457(7225), 76-78, doi:10.1038/nature07650.

Baltzell, C., E. M. Parmentier, Y. Liang, and S. Tirupathi (2015), A high-order numerical study of reactive dissolution in an upwelling heterogeneous mantle: 2. Effect of shear deformation, Geochemistry Geophysics Geosystems, 16(11), 3855-3869, doi:10.1002/2015gc006038.

Bebout, G. E. (2014), Chemical and Isotopic Cycling in Subduction Zones, in Treatise on Geochemistry, edited by H. D. Holland and K. K. Turekian, pp. 703-747, Elsevier.

Beinlich, A., T. John, J. Vrijmoed, M. Tominaga, T. Magna, and Y. Podladchikov (2020), Instantaneous rock transformations in the deep crust driven by reactive fluid flow, Nature Geoscience, 13(4), 307-311.

Bessat, A., S. Pilet, Y. Y. Podladchikov, and S. M. Schmalholz (2022), Melt Migration and Chemical Differentiation by Reactive Porosity Waves, Geochemistry Geophysics Geosystems, 23(2), doi:10.1029/2021gc009963.

Bloch, W., T. John, J. Kummerow, P. Salazar, O. S. Krüger, and S. A. Shapiro (2018), Watching Dehydration: Seismic Indication for Transient Fluid Pathways in the Oceanic Mantle of the Subducting Nazca Slab, Geochemistry, Geophysics, Geosystems, 19(9), 3189-3207, doi:https://doi.org/10.1029/2018GC007703.

Brantut, N., J. Sulem, and A. Schubnel (2011), Effect of dehydration reactions on earthquake nucleation: Stable sliding, slow transients, and unstable slip, Journal of Geophysical Research: Solid Earth, 116(B5).

Burlini, L., G. Di Toro, and P. Meredith (2009), Seismic tremor in subduction zones: Rock physics evidence, Geophysical Research Letters, 36, doi:10.1029/2009gl037735.

Chernak, L. J., and G. Hirth (2010), Deformation of antigorite serpentinite at high temperature and pressure, Earth and Planetary Science Letters, 296(1-2), 23-33, doi:10.1016/j.epsl.2010.04.035.

Connolly, J. (1997), Devolatilization-generated fluid pressure and deformation-propagated fluid flow during prograde regional metamorphism, Journal of Geophysical Research: Solid Earth, 102(B8), 18149-18173.

Connolly, J. (2005), Computation of phase equilibria by linear programming: a tool for geodynamic modeling and its application to subduction zone decarbonation, Earth and Planetary Science Letters, 236(1-2), 524-541.

Connolly, J. (2009), The geodynamic equation of state: What and how, Geochemistry Geophysics Geosystems, 10, doi:10.1029/2009gc002540.

Cruz-Atienza, V. M., C. Villafuerte, and H. S. Bhat (2018), Rapid tremor migration and pore-pressure waves in subduction zones, Nature Communications, 9(1), 2900, doi:10.1038/s41467-018-05150-3.

David, E. C., N. Brantut, L. N. Hansen, and T. M. Mitchell (2018), Absence of Stress-Induced Anisotropy During Brittle Deformation in Antigorite Serpentinite, Journal of Geophysical Research-Solid Earth, 123(12), 10616-10644, doi:10.1029/2018jb016255.

Evans, O., M. Spiegelman, and P. B. Kelemen (2020), Phase-Field Modeling of Reaction-Driven Cracking: Determining Conditions for Extensive Olivine Serpentinization, Journal of Geophysical Research: Solid Earth, 125(1), e2019JB018614.

Fowler, A. C. (1985), A mathematical model of magma transport in the asthenosphere, Geophysical & Astrophysical Fluid Dynamics, 33(1-4), 63-96, doi:10.1080/03091928508245423.

Frank, W. B., N. M. Shapiro, A. L. Husker, V. Kostoglodov, H. S. Bhat, and M. Carnpillo (2015), Along-fault pore-pressure evolution during a slow-slip event in Guerrero, Mexico, Earth and Planetary Science Letters, 413, 135-143, doi:10.1016/j.epsl.2014.12.051.

Gerya, T. (2019), Introduction to numerical geodynamic modelling, Cambridge University Press.

Gomberg, J., Cascadia, and B. W. Group (2010), Slow-slip phenomena in Cascadia from 2007 and beyond: A review, Bulletin, 122(7-8), 963-978.

Hacker, B. R., S. M. Peacock, G. A. Abers, and S. D. Holloway (2003), Subduction factory 2. Are intermediate-depth earthquakes in subducting slabs linked to metamorphic dehydration reactions?, Journal of Geophysical Research: Solid Earth, 108(B1).

Hatakeyama, K., I. Katayama, K.-i. Hirauchi, and K. Michibayashi (2017), Mantle hydration along outer-rise faults inferred from serpentinite permeability, Scientific Reports, 7(1), 13870, doi:10.1038/s41598-017-14309-9.

Hebert, L. B., P. Antoshechkina, P. Asimow, and M. Gurnis (2009), Emergence of a low-viscosity channel in subduction zones through the coupling of mantle flow and thermodynamics, Earth and Planetary Science Letters, 278(3-4), 243-256, doi:10.1016/j.epsl.2008.12.013.

Hermann, J., O. Müntener, and M. Scambelluri (2000), The importance of serpentinite mylonites for subduction and exhumation of oceanic crust, Tectonophysics, 327(3-4), 225-238.

Hilairet, N., B. Reynard, Y. B. Wang, I. Daniel, S. Merkel, N. Nishiyama, and S. Petitgirard (2007), High-pressure creep of serpentine, interseismic deformation, and initiation of subduction, Science, 318(5858), 1910-1913, doi:10.1126/science.1148494.

Hirauchi, K., I. Katayama, and Y. Kouketsu (2020), Semi-brittle deformation of antigorite serpentinite under forearc mantle wedge conditions, Journal of Structural Geology, 140, doi:10.1016/j.jsg.2020.104151.

Holland, T., and R. Powell (1998), An internally consistent thermodynamic data set for phases of petrological interest, Journal of metamorphic Geology, 16(3), 309-343.

Huber, K., J. C. Vrijmoed, and T. John (2022), Formation of Olivine Veins by Reactive Fluid Flow in a Dehydrating Serpentinite, Geochemistry, Geophysics, Geosystems, 23(6), e2021GC010267, doi:https://doi.org/10.1029/2021GC010267.

John, T., N. Gussone, Y. Y. Podladchikov, G. E. Bebout, R. Dohmen, R. Halama, R. Klemd, T. Magna, and H. M. Seitz (2012), Volcanic arcs fed by rapid pulsed fluid flow through subducting slabs, Nature Geoscience, 5(7), 489-492, doi:10.1038/ngeo1482.

Kato, A., et al. (2010), Variations of fluid pressure within the subducting oceanic crust and slow earthquakes, Geophysical Research Letters, 37, doi:10.1029/2010gl043723.

Kempf, E. D., J. Hermann, E. Reusser, L. P. Baumgartner, and P. Lanari (2020), The role of the antigorite + brucite to olivine reaction in subducted serpentinites

(Zermatt, Switzerland) (vol 113, 16, 2020), Swiss Journal of Geosciences, 113(1), doi:10.1186/s00015-020-00377-z.

Kolditz, O., H. Shao, W. Wang, and S. Bauer (2016), Thermo-hydro-mechanical chemical processes in fractured porous media: modelling and benchmarking, 313 pp., Springer, doi:10.1007/978-3-319-11894-9.

Labrousse, L., G. Hetenyi, H. Raimbourg, L. Jolivet, and T. B. Andersen (2010), Initiation of crustal-scale thrusts triggered by metamorphic reactions at depth: Insights from a comparison between the Himalayas and Scandinavian Caledonides, Tectonics, 29, doi:10.1029/2009tc002602.

Llana-Fúnez, S., J. Wheeler, and D. R. Faulkner (2012), Metamorphic reaction rate controlled by fluid pressure not confining pressure: implications of dehydration experiments with gypsum, Contributions to Mineralogy and Petrology, 164(1), 69-79, doi:10.1007/s00410-012-0726-8.

Malvoisin, B., Y. Y. Podladchikov, and A. V. Myasnikov (2021), Achieving complete reaction while the solid volume increases: Anumerical model applied to serpentinisation, Earth and Planetary Science Letters, 563, doi:10.1016/j.epsl.2021.116859.

Matter, J. M., and P. B. Kelemen (2009), Permanent storage of carbon dioxide in geological reservoirs by mineral carbonation, Nature Geoscience, 2(12), 837-841, doi:10.1038/ngeo683.

McKenzie, D. (1984), The generation and compaction of partially molten rock, J. Petrology, 25, 713-765.

Moulas, E., S. M. Schmalholz, Y. Podladchikov, L. Tajčmanová, D. Kostopoulos, and L. Baumgartner (2019), Relation between mean stress, thermodynamic, and lithostatic pressure, Journal of metamorphic geology, 37(1), 1-14.

Omlin, S., B. Malvoisin, and Y. Y. Podladchikov (2017), Pore fluid extraction by reactive solitary waves in 3-D, Geophysical Research Letters, 44(18), 9267-9275.

Pandey, S. N., V. Vishal, and A. Chaudhuri (2018), Geothermal reservoir modeling in a coupled thermo-hydro-mechanical-chemical approach: A review, Earth-Science Reviews, 185, 1157-1169, doi:10.1016/j.earscirev.2018.09.004.

Peacock, S. M. (1990), Fluid processes in subduction zones, Science, 248(4953), 329-337, doi:10.1126/science.248.4953.329.

Peng, Z. G., and J. Gomberg (2010), An integrated perspective of the continuum between earthquakes and slow-slip phenomena, Nature Geoscience, 3(9), 599-607, doi:10.1038/ngeo940.

Peters, D., T. Pettke, T. John, and M. Scambelluri (2020), The role of brucite in water and element cycling during serpentinite subduction – Insights from Erro Tobbio (Liguria, Italy), Lithos, 360-361, 105431, doi:https://doi.org/10.1016/j.lithos.2020.105431.

Pettke, T., and A. Bretscher (2022), Fluid-mediated element cycling in subducted oceanic lithosphere: The orogenic serpentinite perspective, Earth-Science Reviews, 225, doi:10.1016/j.earscirev.2021.103896.

Plümper, O., T. John, Y. Y. Podladchikov, J. C. Vrijmoed, and M. Scambelluri (2017), Fluid escape from subduction zones controlled by channel-forming reactive porosity, Nature Geoscience, 10(2), 150-156.

Poulet, T., A. Karrech, K. Regenauer-Lieb, L. Fisher, and P. Schaubs (2012), Thermal–hydraulic–mechanical–chemical coupling with damage mechanics using ESCRIPTRT and ABAQUS, Tectonophysics, 526, 124-132.

Poulet, T., M. Veveakis, M. Herwegh, T. Buckingham, and K. Regenauer-Lieb (2014), Modeling episodic fluid-release events in the ductile carbonates of the Glarus thrust, Geophysical Research Letters, 41(20), 7121-7128, doi:10.1002/2014gl061715.

Rass, L., D. Kolyukhin, and A. Minakov (2019), Efficient parallel random field generator for large 3-D geophysical problems, Computers & Geosciences, 131, 158-169, doi:10.1016/j.cageo.2019.06.007.

Reiner, M. (1964), The Deborah number, Physics Today, 17(1), 62.

Rupke, L. H., J. P. Morgan, M. Hort, and J. A. D. Connolly (2004), Serpentine and the subduction zone water cycle, Earth and Planetary Science Letters, 223(1-2), 17-34, doi:10.1016/j.epsl.2004.04.018.

Scambelluri, M., J. Fiebig, N. Malaspina, O. Muntener, and T. Pettke (2004), Serpentinite subduction: Implications for fluid processes and trace-element recycling, International Geology Review, 46(7), 595-613, doi:10.2747/0020-6814.46.7.595.

Scambelluri, M., O. Muntener, J. Hermann, G. B. Piccardo, and V. Trommsdorff (1995), Subduction of water into the mantle - history of an Alpine peridotite, Geology, 23(5), 459-462, doi:10.1130/0091-7613(1995)023<0459:Sowitm>2.3.Co;2.

Scambelluri, M., E. H. H. Strating, G. B. Piccardo, R. L. M. Vissers, and E. Rampone (1991), Alpine olivine-bearing and titanium clinohumite-bearing assemblages in the Erro Tobbio peridotite (Voltri-massif, NW Italy), Journal of Metamorphic Geology, 9(1), 79-91, doi:10.1111/j.1525-1314.1991.tb00505.x.

Schiemenz, A., Y. Liang, and E. M. Parmentier (2011), A high-order numerical study of reactive dissolution in an upwelling heterogeneous mantle-I. Channelization, channel lithology and channel geometry, Geophysical Journal International, 186(2), 641-664, doi:10.1111/j.1365-246X.2011.05065.x.

Schmalholz, S. M., E. Moulas, O. Plumper, A. V. Myasnikov, and Y. Y. Podladchikov (2020), 2D Hydro-Mechanical-Chemical Modeling of (De)hydration Reactions in Deforming Heterogeneous Rock: The Periclase-Brucite Model Reaction, Geochemistry Geophysics Geosystems, 21(11), doi:10.1029/2020gc009351.

Schmalholz, S. M., and L. Räss (2022), PTsolvers/PseudoTransientHMC.jl: PseudoTransientHMC.jl 0.1.0 (v0.1.0), edited, Zenodo, doi:https://doi.org/10.5281/zenodo.6559431.

Schmeling, H., J. P. Kruse, and G. Richard (2012), Effective shear and bulk viscosity of partially molten rock based on elastic moduli theory of a fluid filled poroelastic medium, Geophysical Journal International, 190(3), 1571-1578, doi:10.1111/j.1365-246X.2012.05596.x.

Shelly, D. R., G. C. Beroza, and S. Ide (2007), Non-volcanic tremor and low-frequency earthquake swarms, Nature, 446(7133), 305-307.

Spitz, R., S. M. Schmalholz, B. J. Kaus, and A. A. Popov (2020), Quantification and visualization of finite strain in 3D viscous numerical models of folding and overthrusting, Journal of Structural Geology, 131, 103945.

Sulem, J., and V. Famin (2009), Thermal decomposition of carbonates in fault zones: Slip-weakening and temperature-limiting effects, Journal of Geophysical Research: Solid Earth, 114(B3).

Taetz, S., T. John, M. Brocker, C. Spandler, and A. Stracke (2018), Fast intraslab fluid-flow events linked to pulses of high pore fluid pressure at the subducted plate interface, Earth and Planetary Science Letters, 482, 33-43, doi:10.1016/j.epsl.2017.10.044.

Tarling, M. S., S. A. F. Smith, and J. M. Scott (2019), Fluid overpressure from chemical reactions in serpentinite within the source region of deep episodic tremor, Nature Geoscience, 12(12), 1034-1042, doi:10.1038/s41561-019-0470-z.

Ulmer, P., and V. Trommsdorff (1995), Serpentine Stability to Mantle Depths and Subduction-Related Magmatism, Science, 268(5212), 858-861, doi:doi:10.1126/science.268.5212.858.

Van Avendonk, H. J. A., W. S. Holbrook, D. Lizarralde, M. M. Mora, S. Harder, A. D. Bullock, G. E. Alvarado, and C. J. Ramirez (2010), Seismic evidence for fluids in fault zones on top of the subducting Cocos Plate beneath Costa Rica, Geophysical Journal International, 181(2), 997-1016, doi:10.1111/j.1365-246X.2010.04552.x.

Wang, L. H., V. M. Yarushina, Y. Alkhimenkov, and Y. Podladchikov (2021), Physics-inspired pseudo-transient method and its application in modelling focused fluid flow with geological complexity, Geophysical Journal International, 229(1), 1-20, doi:10.1093/gji/ggab426.

Yarushina, V. M., and Y. Y. Podladchikov (2015), (De) compaction of porous viscoelastoplastic media: Model formulation, Journal of Geophysical Research: Solid Earth, 120(6), 4146-4170.

Figures with captions

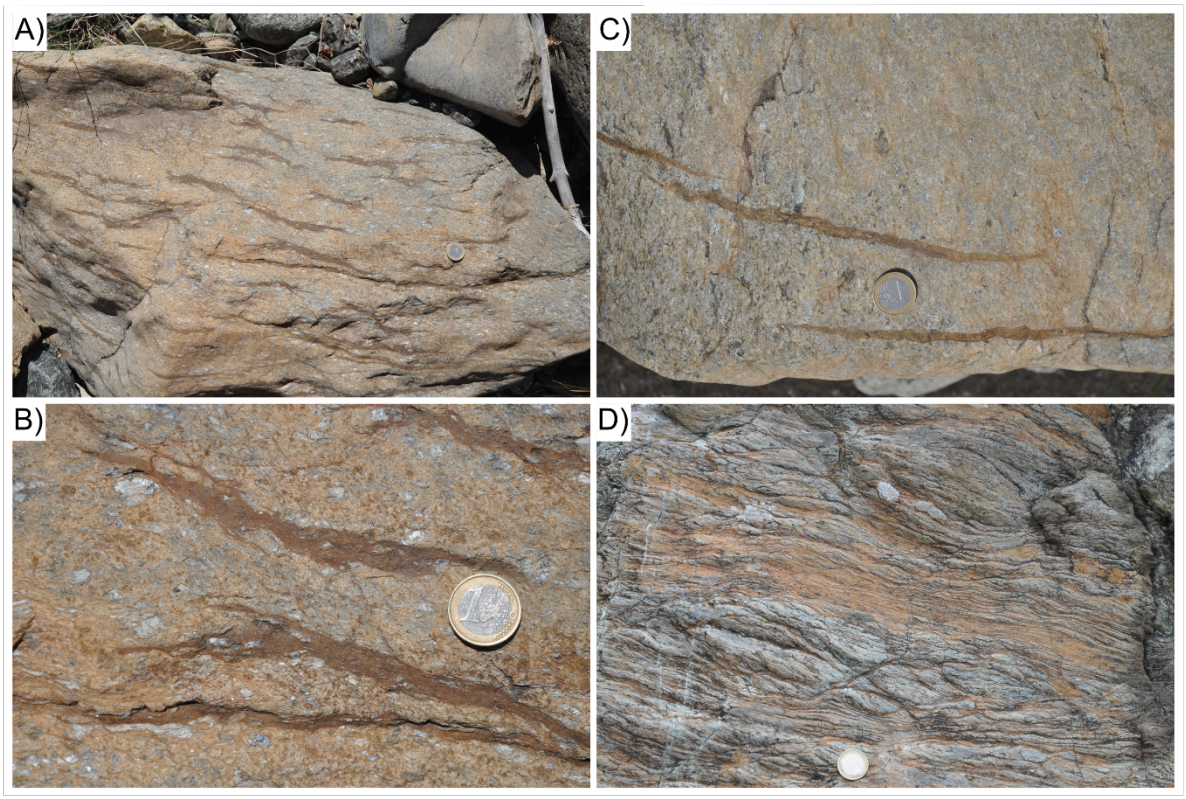

Figure 1. Natural examples of metamorphic olivine veins in antigorite serpentinite from the Erro Tobbio ultramafic rocks, Ligurian Alps, Italy. A) Overview on the limited spatial extent of olivine bearing veins (with darker color) in weakly deformed serpentinized peridotite. Coin diameter is 2.4 cm. B) Olivine veins with characteristic spacing and aspect ratios in serpentinised peridotite. Detail of picture in A). C) olivine-bearing veins in a serpentinised peridotite, foliation is sub vertical, extent of veins is ca. 20 cm. D) Serpentinite mylonite with different generations of olivine veins. An earlier set is subparallel to the foliation, younger shear bands dissect serpentinite mylonite and olivine veins. Top-to-the-left shear sense. Note the late stage serpentine veins perpendicular to the foliation.

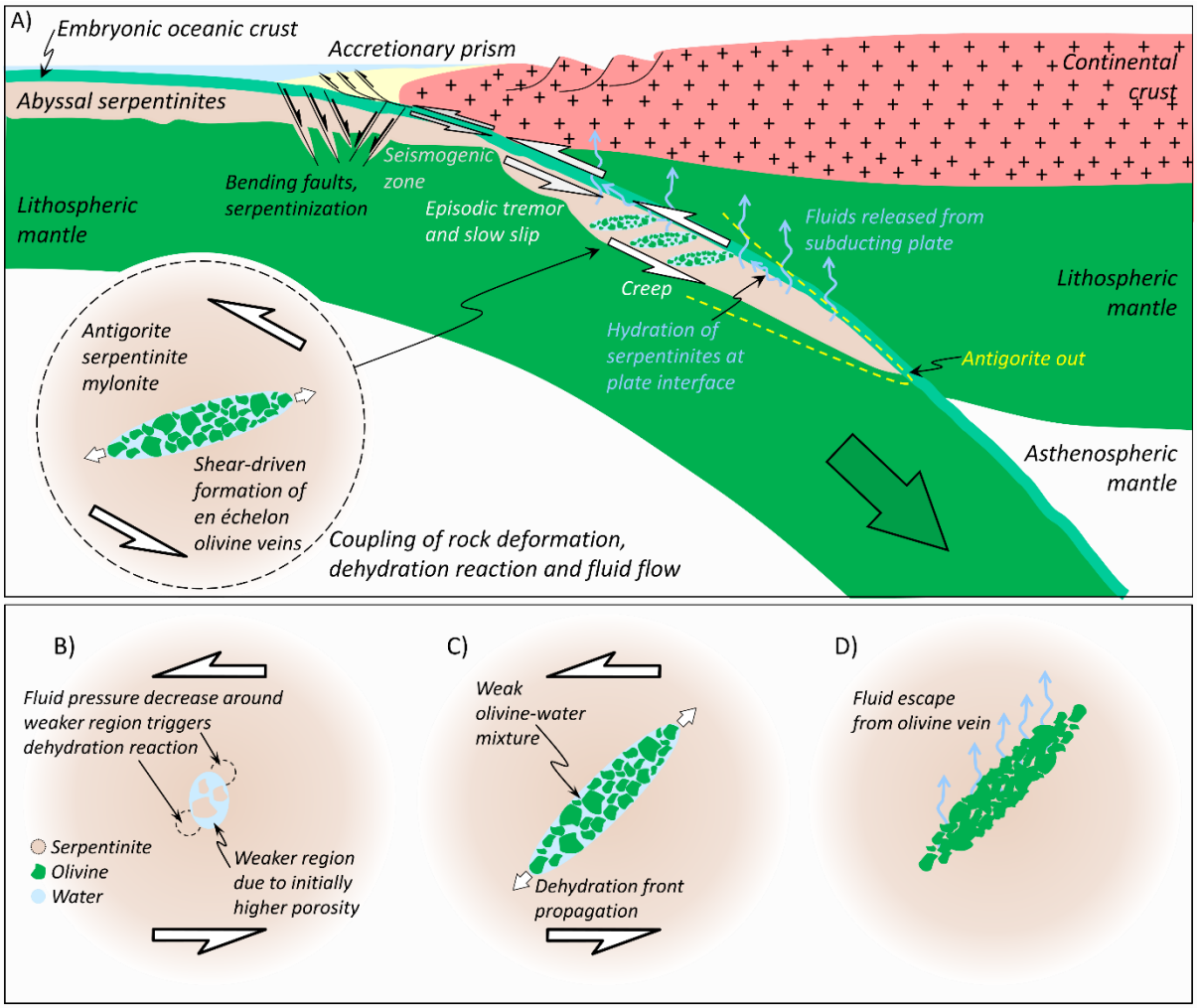

Figure 2. Simple sketches illustrating the geodynamic setting (A) and the hypothesis for shear-driven dehydration and olivine vein formation in viscous serpentinite (B to D; see text for details).

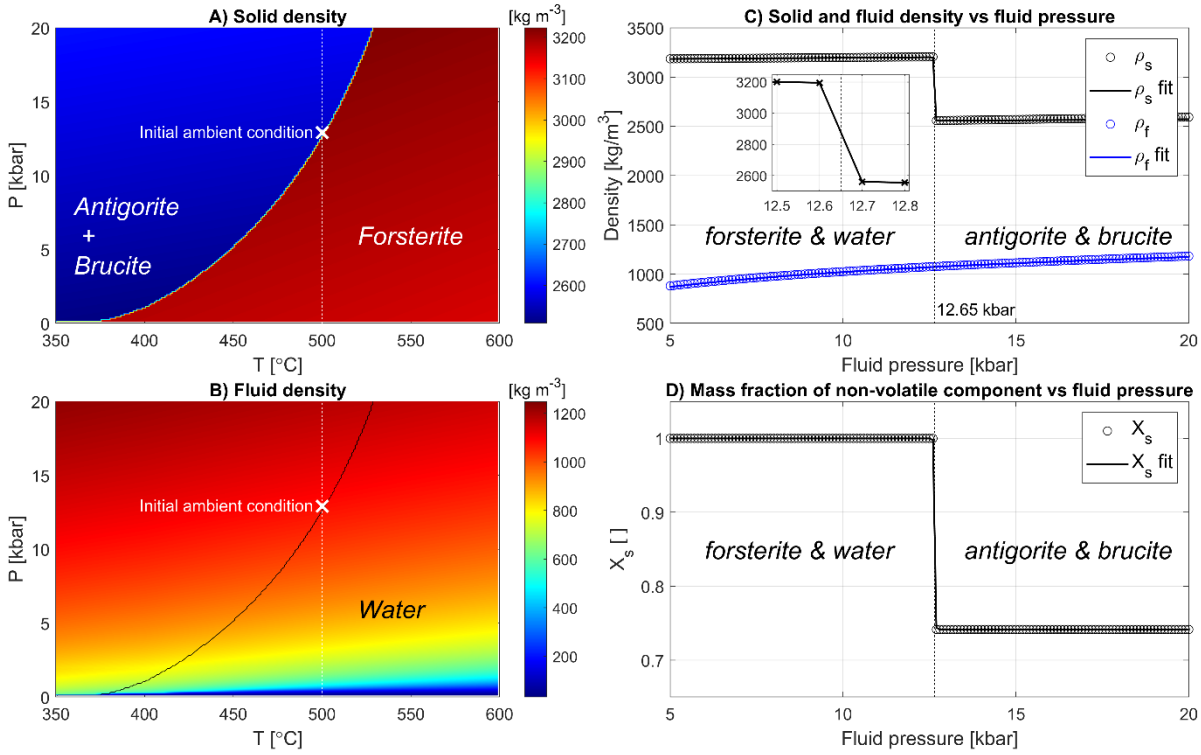

Figure 3. Thermodynamic results obtained from Gibbs' free energy minimization for the system antigorite + brucite = forsterite + water (see text for exact chemical formulas). Density fields of solid (A) and fluid (B) in thermodynamic pressure, , and temperature, , space. Corresponding profiles of solid and fluid densities (C) and mass fraction of MgO (D) as a function of fluid pressure at 500 °C. The circles in the three profiles in panels C) and D) are the results from Gibbs energy minimization and the corresponding solid lines are analytical approximations of these profiles (equation), which are used in the numerical algorithm.

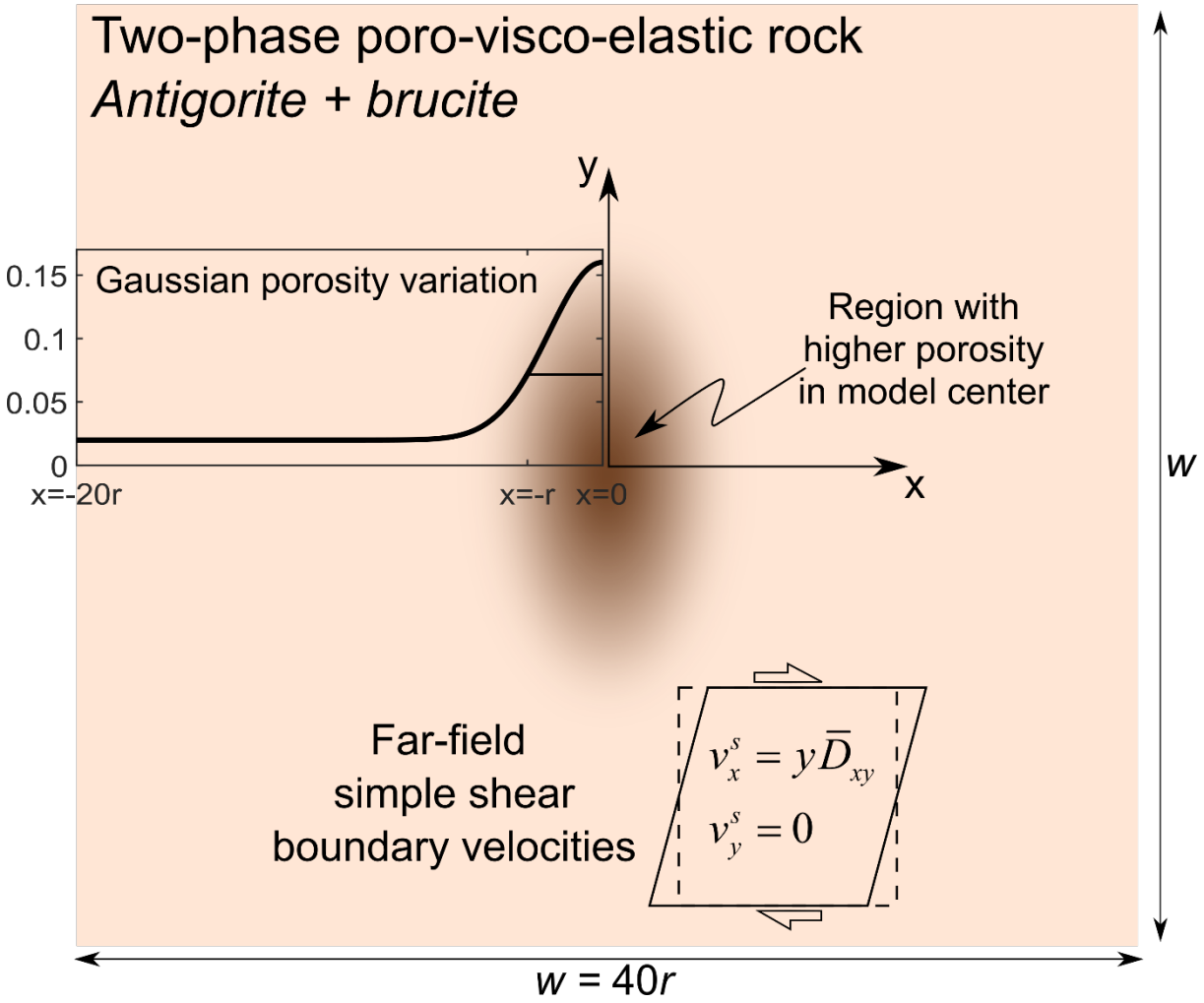

Figure 4. Sketch of the model configuration and the applied far-field simple shear (bottom right sketch; see text for details). The intitial distribution of the porosity is described by a 2D Gaussian distribution, having an initial horizontal bandwidth of 2 (graph in left middle of the sketch) and a vertical bandwidth of 4. The width and height of the model is 40 and the applied far-field shearing rate is .

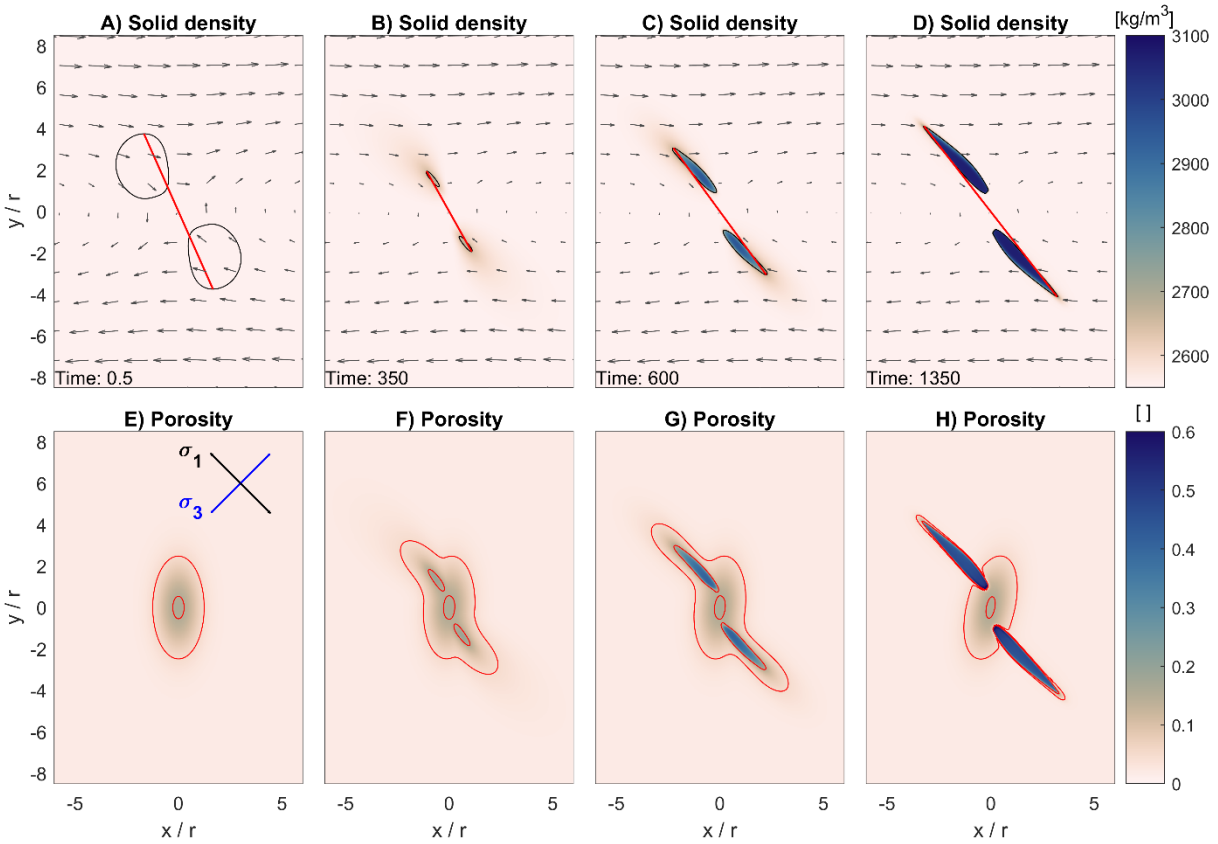

Figure 5. Representative evolution of a dehydration vein under simple shear for a simulation with = 0.071 and = 0.0025. Panels A) to D) show snapshots of solid density for four stages of the simulation, indicated by a dimensionless time (see text). The black contour lines in panels A) to D) indicated the contour for = 12.65 kbar (is smaller inside the contour), which is the thermodynamic pressure at the dehydration reaction (see Fig. 3). Grey arrows indicate the solid velocities which are dominated by the applied simple shear. The red line connects the highest with the lowest point of the fluid pressure contours and the length of the red line is used as proxy to monitor the vein growth with time. Panels E) to H) show the porosity corresponding to the model times of panels A) to D). In panel E), the black line indicates the direction of the maximal principal stress, , and the blue line indicates the direction of the minimal principal stress, , at the location of the intersection of the two lines. The red contours indicate a porosity of 5% (outer contour) and 15% (inner contour).

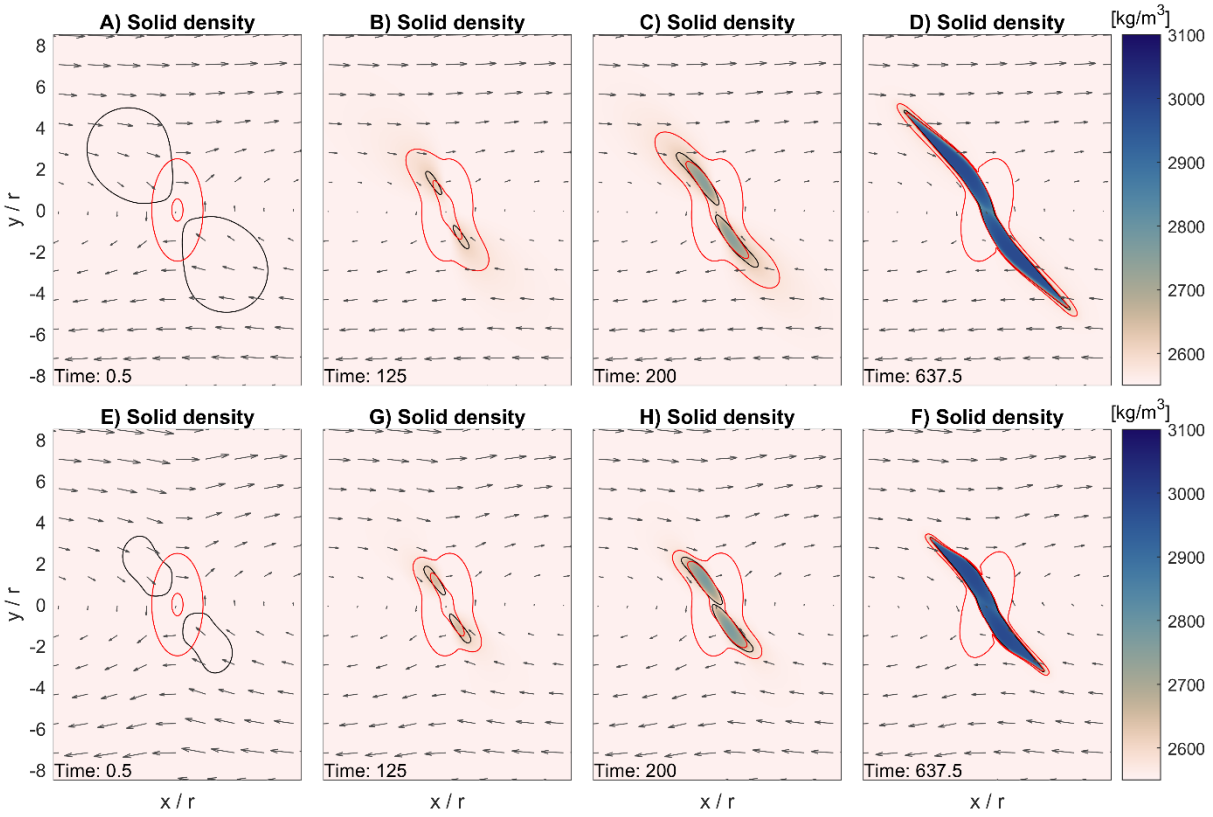

Figure 6. Representative evolution of dehydration veins under simple shear for two simulations with = 0.038 and = 0.0025. Colomaps indicate the solid density. The simulation shown in panels A) to D) is purely viscous whereas for the simulation shown in E) to F) a von Mises yield stress of 150 MPa was applied and deformation is visco-plastic. In all panels, the black contour lines indicate the contour for = 12.65 kbar (is smaller inside the contour), the grey arrows indicate the solid velocities and the red contours indicate a porosity of 5% (outer contour) and 15% (inner contour).

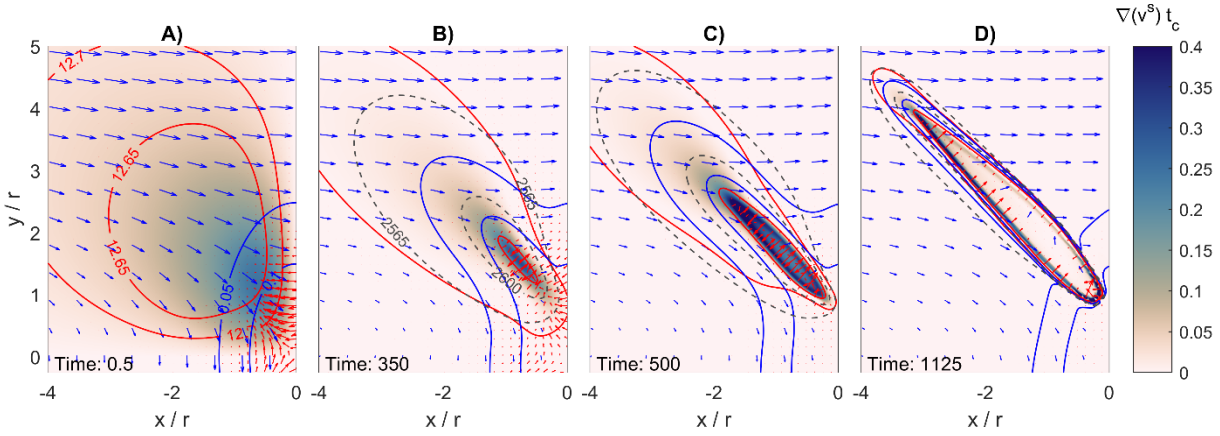

Figure 7. Evolution of a dehydration vein under simple shear for a simulation (shown in Fig. 5) with = 0.071 and = 0.0025 at four dimensionless times (see text). The colormaps show the dimensionless divergence of the solid velocity, the red arrows show the fluid velocity field and the blue arrows show the solid velocity field. The two red contours indicate = 12.65 (always the inner contour) and 12.7 kbar. The two blue contours indicate a porosity of 5% (outer contour) and 10% (inner contour). The two dashed grey contours indicate a solid density of 2565 kg/m^3 (outer contour) and 2600 kg/m^3 (inner contour). There are no solid density contours in panel A) because all densities are < 2565 kg/m^3.

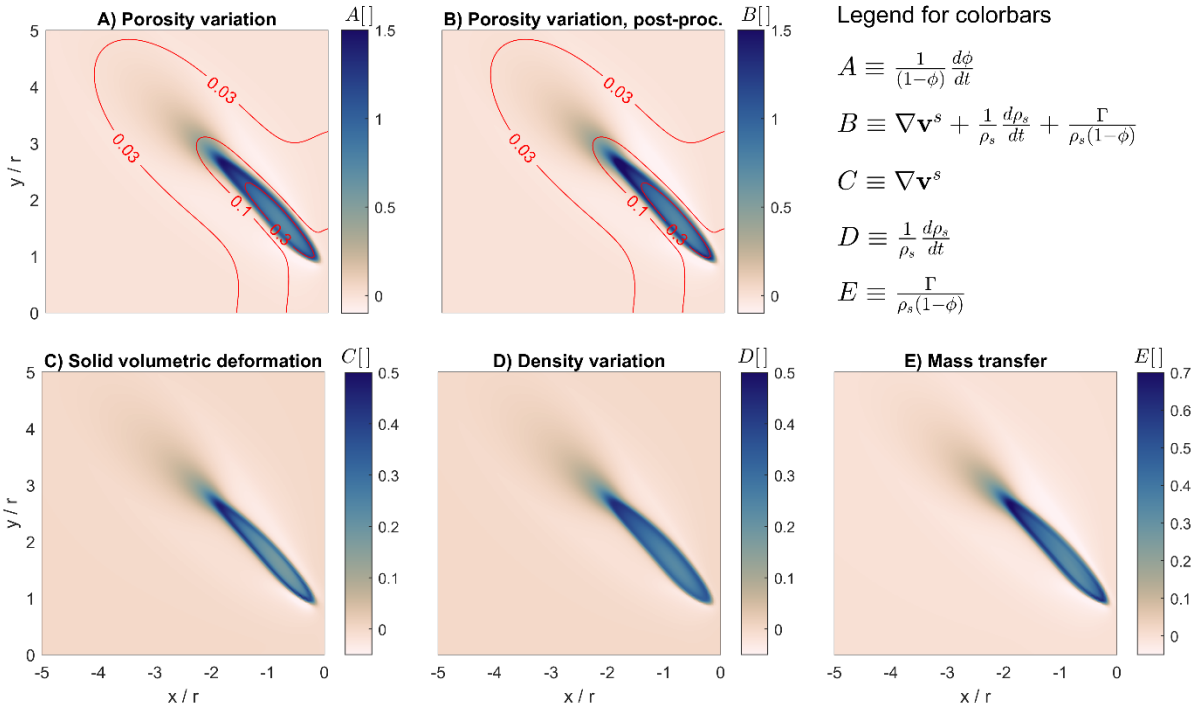

Figure 8. The three mechanisms (solid volumetric deformation, C, solid-density variation, D, and mass transfer, E) that control the temporal porosity variation (see equation) for a simulation (shown in Fig. 5) with = 0.071 and = 0.0025 at a dimensionless time of 550. A) shows the colormap of the term displayed in the legend for A, B) shows the colormap of the term displayed in the legend for B, C) shows the colormap of the term displayed in the legend for C, D) shows the colormap of the term displayed in the legend for D and E) shows the colormap of the term displayed in the legend for E. All displayed terms represent dimensionless rates which can be made dimensionless by multiplying with the characteristic time, (see text).

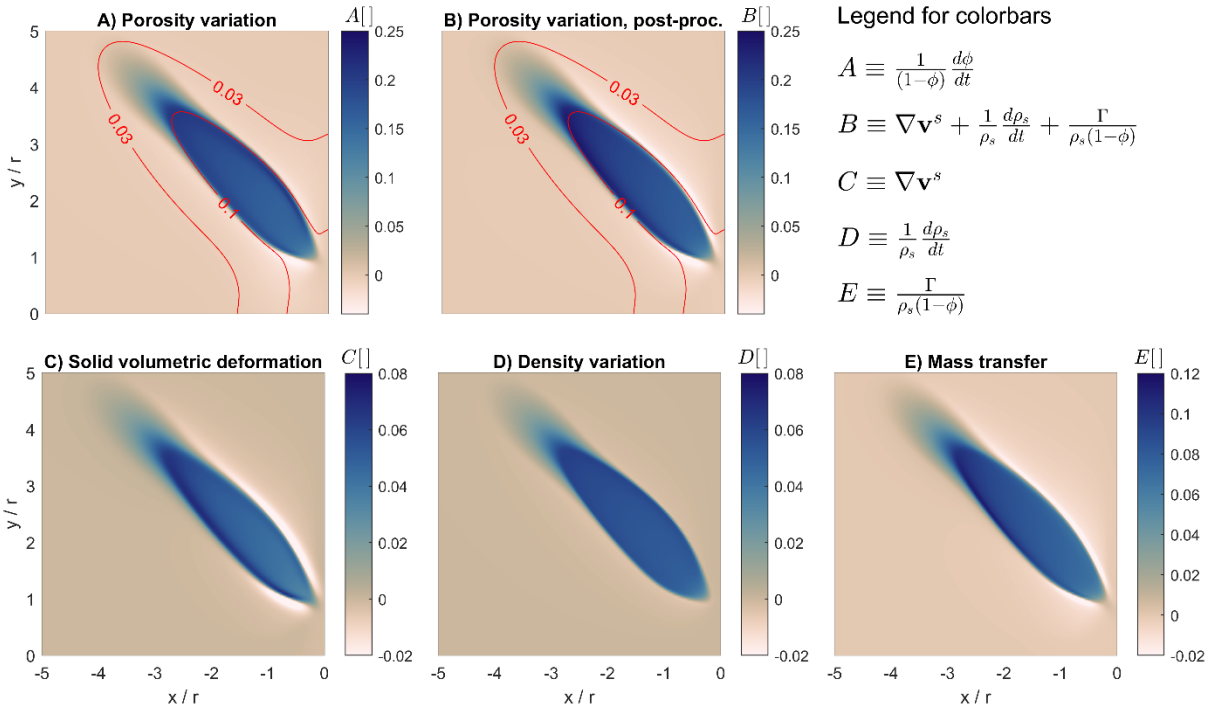

Figure 9. The three mechanisms (solid volumetric deformation, C, solid-density variation, D, and mass transfer, E) that control temporal porosity variation (see equation) for a simulation with = 0.071 and = 0.022 at a dimensionless time of 800. A) shows the colormap of the term displayed in the legend for A, B) shows the colormap of the term displayed in the legend for B, C) shows the colormap of the term displayed in the legend for C, D) shows the colormap of the term displayed in the legend for D and E) shows the colormap of the term displayed in the legend for E. All displayed terms represent dimensionless rates which can be made dimensionless by multiplying with the characteristic time, (see text).

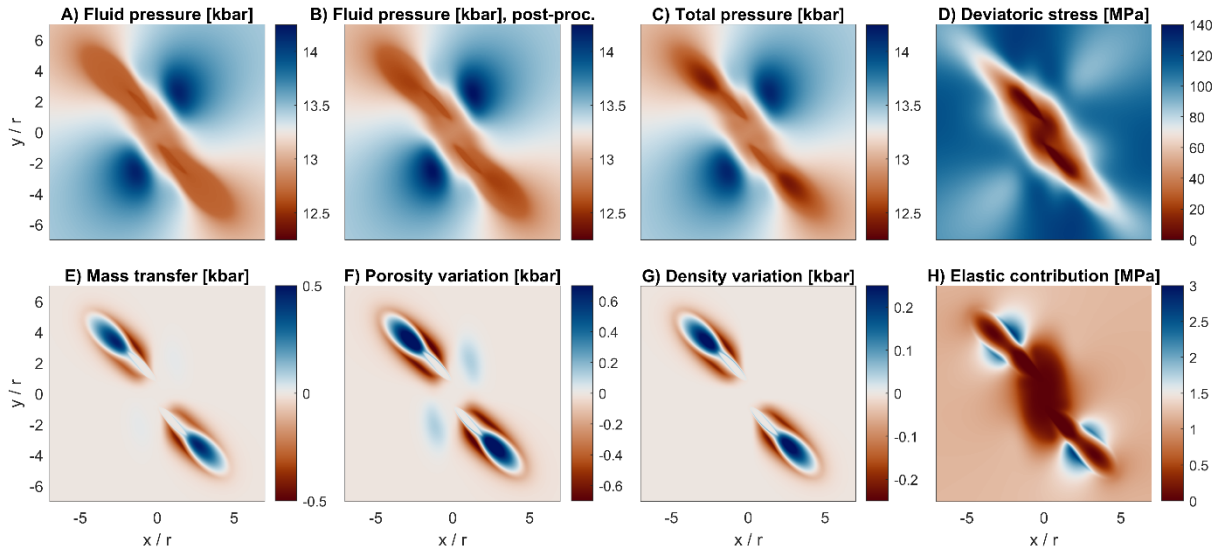

Figure 10. The five mechanisms and quantities that control the distribution of fluid pressure (equation) for a simulation (shown in Fig. 5) with = 0.071 and = 0.0025 at a dimensionless time of 550. A) Colormap of fluid pressure which was calculated by the numerical simulation and B) fluid pressure which was post-processed from numerical results using equation . C) shows the total pressure and D) the deviatoric stress, , which was calculated by the numerical simulation. E) shows the contribution to the fluid pressure due to mass transfer (last term on right-hand side of equation), F) due to porosity variation (third term on right-hand side of equation), G) due to solid density variation (fourth term on right-hand side of equation) and H) due to elastic deformation (second term on right-hand side of equation). All quantities displayed in E) to H) have been post-processed from numerical results.

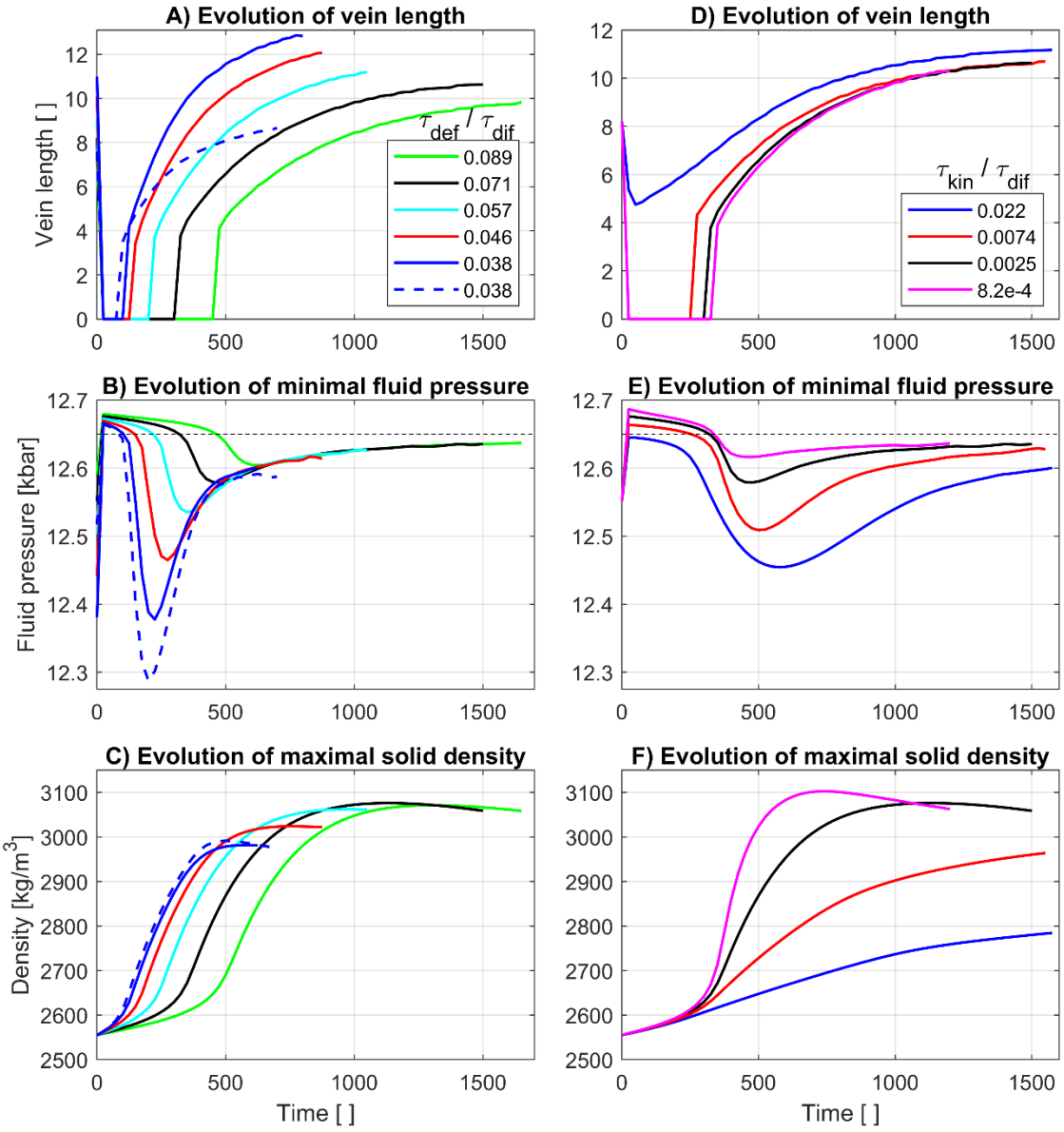

Figure 11. Impact of far-field shearing rate (A to C) and kinetic reaction rate (B to F) on the evolution of vein length (A and D), on the minimal value of the fluid pressure in the model domain (B and E) and on the evolution of the maximal solid density in the model domain (C and F). For the results displayed in panels A) to C) the ratio = 0.0025 for all simulations. For the results displayed in panels D) to F) the ratio = 0.071 for all simulations. Results indicated with the dashed blue line are obtained by the same simulation which provided results indicated by the solid blue line, but with a von Mises yield stress of 150 MPa

(results of the two simulations are also displayed in Fig. 6).

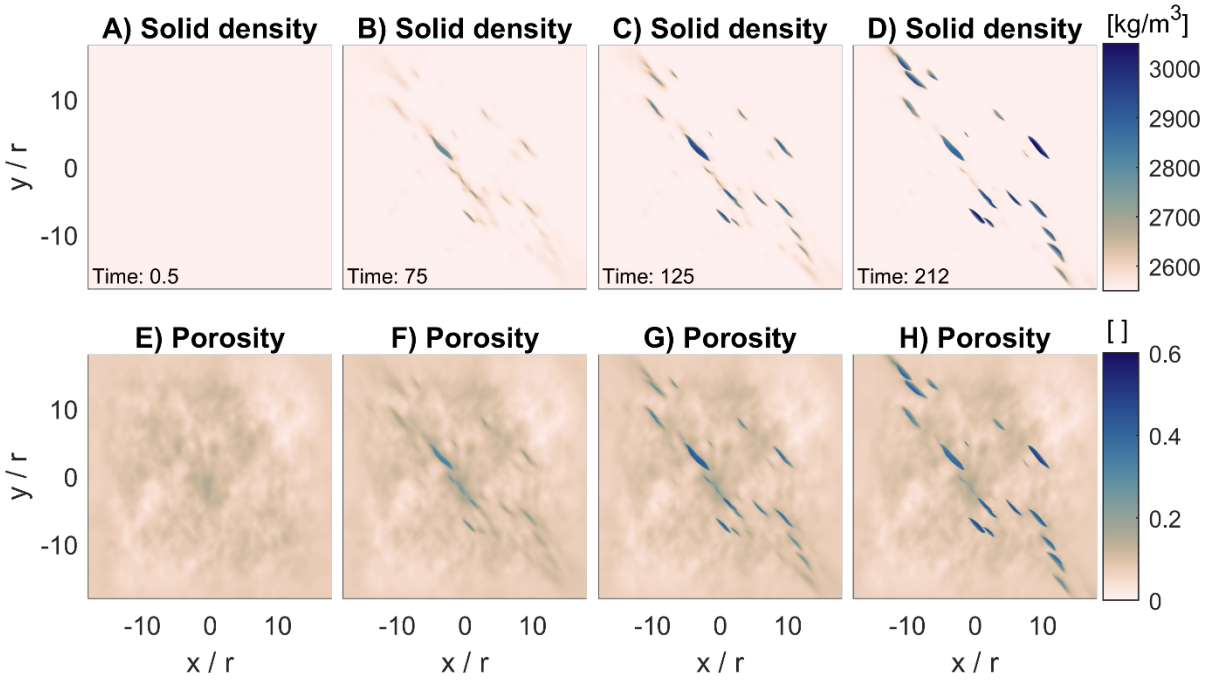

Figure 12. Evolution of solid density (A to D) and corresponding porosity (E to H) for a simulation with an initial random distribution of porosity (see Discussion).

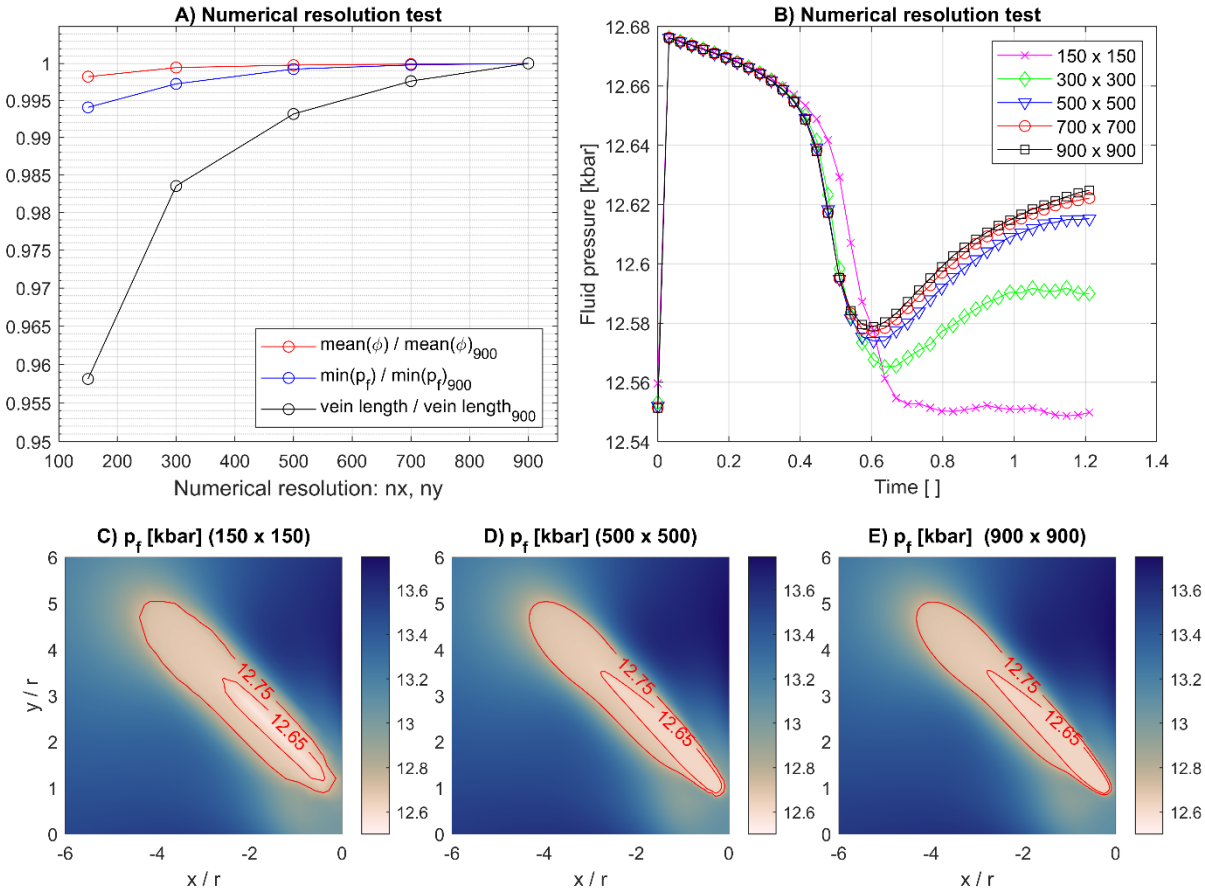

Figure A1. Numerical resolution test for the simulation with = 0.071 and = 0.0025 (see Fig. 5). A) For a dimensionless model time of 1.21, the ratio of the mean porosity in the model domain divided by the mean porosity for a simulation with a resolution of 900 × 900 grid points is plotted versus the corresponding resolution for simulations with different resolution. Similar ratios are plotted for the minimum fluid pressure in the model domain and the vein length. The larger the resolution, the less the three ratios vary. B) Evolution of minimum fluid pressure in the model domain with time for different numerical resolutions (see legend). With larger resolution, the evolution of fluid pressure varies less. C) to D) At a dimensionless model time of 1.0, the colormap of the fluid pressure is displayed for three different resolutions (see numbers in panel titles). Two contour lines of fluid pressure are displayed for better comparability.

Table 1. Model variables and parameters.

Symbol	Name / Definition	Units
	Kinetic time scale	

Symbol	Name / Definition	Units
	Fluid pressure	
	Porosity	
	Initial porosity	
	Solid density	
	Fluid density	
	Mass fraction MgO	
	Total pressure	
,	Solid velocities	
,	Fluid velocities	
„	Deviatoric stresses	
	Permeability	
	Fluid viscosity	
	Shear viscosity solid	
	Bulk viscosity solid	
	Bulk modulus solid	
	Bulk modulus drained	
	Initial ambient pressure	
	Far-field deformation rate	
	Bandwidth of Gaussian	
	Model width	